LLNL-CONF-404196

LAWRENCE
LIVERMORE
NATIONAL
LABORATORY

Ray-Based Calculations with DEPLETE of Laser Backscatter in ICF Targets

D. J. Strozzi, E. Williams, D. Hinkel, D. Froula, R. London, D. Callahan

May 28, 2008

38th Anomalous Absorption Conference
Williamsbirg, VA, United States
June 1, 2008 through June 6, 2008

Disclaimer

Ray-Based Calculations with DEPLETE of Laser Backscatter in ICF Targets

D. J. Strozzi, E. A. Williams, D. E. Hinkel, D. H. Froula, R. A. London, D. A. Callahan

Lawrence Livermore National Laboratory, Livermore, CA, 94550 USA

A steady-state model for Brillouin and Raman backscatter along a laser ray path is presented. The daughter plasma waves are treated in the strong damping limit, and have amplitudes given by the (linear) kinetic response to the ponderomotive drive. Pump depletion, inverse-bremsstrahlung damping, bremsstrahlung emission, Thomson scattering off density fluctuations, and whole-beam focusing are included. The numerical code Deplete, which implements this model, is described. The model is compared with traditional linear gain calculations, as well as "plane-wave" simulations with the paraxial propagation code pF3D. Comparisons with Brillouin-scattering experiments at the Omega Laser Facility show that laser speckles greatly enhance the reflectivity over the Deplete results. An approximate upper bound on this enhancement is given by doubling the Deplete coupling coefficient. Analysis with Deplete of an ignition design for the National Ignition Facility (NIF), with a peak radiation temperature of 285 eV, shows encouragingly low reflectivity. Doubling the coupling to bracket speckle effects suggests a less optimistic picture. Re-absorption of Raman light is seen to be significant in this design.

Poster P1-8
2 June 2008
38th Anomalous Absorption Conference
Williamsburg, VA USA

NIC
The National Ignition Campaign

This work performed under the auspices of the U.S. Department of Energy by Lawrence Livermore National Laboratory under Contract DE-AC52-07NA27344

LLNL-CONF-404196

1 Introduction

Laser-plasma interaction (LPI) [1] is an important plasma-physics problem which poses serious challenges to theoretical modeling. LPI is the basis of several applications, including laser-based particle acceleration [2] and the backward Raman amplifier [3]. Moreover, for inertial confinement fusion (ICF)[4, 5] to succeed, LPI must not be so active that it prevents the desired laser energy from being delivered to the target, with the desired spatial and temporal behavior. This paper focuses on modeling the backscatter instabilities, where a laser light wave (mode 0) decays into a backscattered light wave (mode 1) and a plasma wave (mode 2). In stimulated Raman scattering (SRS) and stimulated Brillouin scattering (SBS), the plasma wave is, respectively, an electron plasma wave and an ion acoustic wave. These are the LPI processes presently considered to pose the largest risk to indirect-drive ICF [5].

A wide array of computational tools is used to model LPI, ranging from rapid (∼secs) calculations of linear gains along 1D "ray" profiles to massively-parallel kinetic particle-in-cell simulations. We present here a new tool, called DEPLETE, to the less computationally expensive end of this spectrum. DEPLETE solves for the pump intensity and scattered-wave spectral density for a set of scattered frequencies, in steady-state, along a 1D profile of plasma conditions. Pump depletion is included, and the plasma waves are assumed to be in the strong damping limit (i.e., they do not advect). Fully kinetic (although linear) formulas are used for various quantities like the coupling coefficient. Bremsstrahlung noise and damping, as well as Thomson scattering (TS), are included. The DEPLETE model, especially the noise sources, in some ways resembles that of Ref. [6]. Other similar works which have influenced our thinking, and use 1D coupled-mode equations, are Refs. [7]-[8].

DEPLETE is similar to the code NEWLIP, which calculates linear gains for SRS and SBS along 1D profiles (NEWLIP is briefly discussed on p. 13 of Ref. [9], and also here in Appendix A). Both codes run very quickly, taking seconds or less to analyze one ray path from the laser entrance to the high-Z wall in an ICF ignition design. However, DEPLETE includes substantially more physics than NEWLIP, such as pump depletion, bremsstrahlung and Thomson noise sources, and re-absorption of the scattered waves. DEPLETE moreover provides pump and scattered intensities, which unlike gains can be directly compared with experiment and more sophisticated LPI codes. Despite its simplicity, DEPLETE nonetheless agrees well in certain cases with results from the 3D paraxial laser propagation code pF3D. This is quite promising given DEPLETE's much lower computing cost. The favorable comparison also vindicates the use of the simple 1D models embodied in NEWLIP and DEPLETE.

There is important physics which DEPLETE does not capture, with laser speckles or hot spots being one of the most important. Recent SBS experiments [10, 11] at the Omega Laser Facility [12] show good agreement between measured reflectivity and pF3D predictions, while DEPLETE gives a lower value. Sec. 7 describes a crude way to put an upper bound on speckle effects by doubling the coupling coefficient; the two DEPLETE reflectivities then bracket the experimental results. A more sophisticated idea for handling speckles is outlined in the conclusion. DEPLETE with its unmodified coupling coefficient gives a lower bound on the reflectivity of a speckled, phase-plate-smoothed, laser beam. Additional beam smoothing, like polarization smoothing (PS) and smoothing by spectral dispersion (SSD), reduce the effective speckle intensity and can reduce the reflectivity even below the speckle-free DEPLETE level.

The paper is organized as follows. Section 2 presents the governing equations, starting with equations for quasi-monochromatic complex wave amplitudes and ending with equations for the pump intensity and scattered-wave spectral density. The numerical method is given in Sec. 3, including a quasi-analytic solution for the coupling-Thomson step. Section 4 compares DEPLETE with NEWLIP linear gains and pF3D "plane-wave" simulations on prescribed profiles with linear gradients in plasma conditions. The relationship between Thomson scattering and linear gain is discussed in Sec. 5. We show in Sec. 6 that doubling DEPLETE's coupling coefficient brackets the experimental and pF3D SBS reflectivities in recent Omega shots. In Sec. 7, we use DEPLETE to analyze a 285 eV NIF ignition design; in particular, we show the effect of scattered light re-absorption and put a bound on speckle effects. We conclude and discuss future prospects in Sec. 8. A review of NEWLIP is presented in Appendix A, including the precise definition of its linear gain G_l. Appendix B gives details of the numerical method for solving DEPLETE's coupling-Thomson step.

2 Governing equations

Our approach is to derive coupled-mode equations, in time and one space dimension, for the slowly-varying, quasi-monochromatic complex wave envelopes, and find the resulting intensity equations. We do this for the light waves first, and then the plasma wave in the strong damping limit. We take these equations in steady state to apply independently at each scattered frequency, and transition to a spectrum of scattered light per angular frequency. This may be viewed as a "completely incoherent" treatment of the scattered light at different frequencies. Bremsstrahlung damping and fluctuations, and TS, are then added phenomenologically. Focusing of the whole beam is finally accounted for, giving the system DEPLETE solves. This lengthy section culminates in the DEPLETE system, Eqs. (55-56), on which some readers may wish to focus.

2.1 light-wave action equations

Let z represent the distance along the ray path, and assume all wave vectors and gradients are in that direction ($\partial_x = \partial_y = 0$). $z = 0$ is taken as the left edge of the domain (the "laser entrance"), where we specify the right-moving pump laser; we also specify boundary values for the left-moving backscattered wave at the right edge $z = L_z$. The light waves are linearly polarized in y and represented by their vector potentials $\vec{A}_i = (1/2)A_i(z,t)\hat{y}e^{i\psi_i} + cc$, where $i = 0, 1$ for the pump and scattered wave, respectively. A_i is the slowly-varying complex envelope, and we use the dimensionless $a_i \equiv eA_i/(m_e c)$. $\psi_i(z,t)$ is the rapidly-varying phase with $k_i \equiv \partial_z\psi_i$ and $\omega_i \equiv -\partial_t\psi_i$. Let $\sigma_i \equiv k_i/|k_i|$ with $\sigma_0 = \sigma_2 = +1$ and $\sigma_1 = -1$ (appropriate for backscatter). Thermal fluctuations in the plasma give rise to both light waves and plasma waves. However, upon appropriate averaging the *field amplitudes* of these fluctuations vanish (but their *mean squares* do not). The amplitudes A_i (and n_{j2} below) represent only the coherent, and not the noise, components of the fields. We insert a bremsstrahlung noise source and TS to the intensity equations below.

From the Maxwell equations, A_y, the y component of the total vector potential $\vec{A} = \vec{A}_0 + \vec{A}_1$, satisfies

$$\left[\partial_{tt} - c^2\partial_{zz}\right] A_y = \frac{e}{\epsilon_0}\tilde{n}_e v_{ye}. \tag{1}$$

We work in the Coulomb gauge $\nabla \cdot \vec{A} = 0$. $\tilde{n}_j = n_j + N_{j2}$ is the total number density for species j ($j = e$ for electrons, i for any ion species), $N_{j2} = (1/2)n_{j2}e^{i\psi_2} + cc$, and n_{j2} is the slowly-varying plasma-wave envelope. We define $\omega_{pj} \equiv [n_j Z_j^2 e^2/\epsilon_0 m_j]^{1/2}$, $v_{Tj} \equiv [T_j/m_j]^{1/2}$ and $\lambda_{Dj} \equiv v_{Tj}/\omega_{pj}$, with Z_j the charge state. As usual, the ions are treated as fixed in the transverse current term on the RHS of Eq. (1) due to their large mass. (We look forward to a circumstance where a positively-charged species must be considered mobile, such as an electron-positron plasma!) We use conservation of canonical transverse momentum to relate v_{ye} and A_y: $m_e v_{ye} = eA_y$. This yields

$$\left[\partial_{tt} - c^2\partial_{zz} + \omega_{pe}^2\right] A_y = -\omega_{pe}^2\frac{n_{e2}}{n_e}A_y. \tag{2}$$

To derive the envelope equations, we introduce the small ordering parameter δ:

$$\begin{aligned}\delta &\sim \omega_i^{-1}\partial_t \ln(A_i, k_i, \omega_i, n_e) && (3)\\ &\sim k_i^{-1}\partial_x \ln(A_i, k_i, \omega_i, n_e). && (4)\end{aligned}$$

Formally, we order $\partial_t, \partial_x \sim \delta$ and $\psi_i \sim \delta^{-1}$ in Eq. (2). See Sec. III of Ref. [13] for details. In addition, we take the coupling on the right-hand side to be order δ. To leading order (δ^0), we obtain the free-wave dispersion relation

$$\omega_i^2 = \omega_{pe}^2 + c^2k_i^2 \qquad i = 0, 1. \tag{5}$$

Although this is a nonlinear PDE for ψ_i, for steady-state conditions considered below we take ω_i to be constant and find the eikonal $ck_i(x) = \sigma_i\eta_i\omega_i$ with $\eta_i \equiv [1 - n_e/n_{ci}]^{1/2}$ the index of refraction and $n_{ci} \equiv \omega_i^2\epsilon_0 m_e/e^2$ the critical density of mode i. Also, the group velocity $v_{gi} \equiv \sigma_i\eta_i c$. Our analysis generally assumes $\omega_{0,1} > \omega_{pe}$. To include regions where this is not the case (especially SRS from profiles extending to $\omega_{pe} \gtrsim \omega_0/2$), we gracefully "turn off" certain coefficients and set the wave intensities to zero.

The order δ terms in Eq. (2) yield the envelope equations. The order δ^2 terms contain second derivatives of the envelope and are neglected. We also assume perfect phase matching: $k_0 = k_1 + k_2$ and $\omega_0 = \omega_1 + \omega_2$. Collecting only the resonant terms gives

$$L_0 a_0 = -\frac{i}{4}\frac{\omega_{pe}^2}{\omega_0}\frac{n_{e2}}{n_e}a_1, \tag{6}$$

$$L_0 a_1 = -\frac{i}{4}\frac{\omega_{pe}^2}{\omega_1}\frac{n_{e2}^*}{n_e}a_0. \tag{7}$$

The operator $L_i \equiv \partial_t + v_{gi}\partial_z + (1/2\omega_i)(\partial_t\omega_i + c^2\partial_z k_i)$. Slow variation in k_i and ω_i is needed to correctly recover the standard action-evolution equations, which we presently derive.

For our quasi-monochromatic (slowly-varying) light waves ($i = 0, 1$), the action density [14] is $N_i \equiv (m_e/8\pi r_e)\omega_i a_i a_i^*$ where $r_e \equiv (e^2/4\pi\epsilon_0)/m_e c^2 \approx 2.82$ fm is the classical electron radius. We also define the (positive) action flux $Z_i \equiv N_i|v_{gi}|$ and intensity $I_i \equiv \omega_i Z_i$. In practical units,

$$|a_i|^2 = \frac{I_i\lambda_i^2}{P_{em}\eta_i} \tag{8}$$

where $\lambda_i \equiv 2\pi c/\omega_i$ and $P_{em} \equiv (\pi/2)m_e c^3/r_e \approx 1.368 \times 10^{18}$ W$\cdot$cm^{-2} $\cdot$ μm^2. We form Eq. (6)$\times a_0^* + cc$ and Eq. (7)$\times a_1^* + cc$ to find

$$\partial_t N_0 + \partial_z Z_0 = -J, \tag{9}$$

$$\partial_t N_1 - \partial_z Z_1 = J, \tag{10}$$

$$J \equiv -\frac{1}{4}m_e c^2 \,\mathrm{Im}[a_0^* a_1 n_{e2}]. \tag{11}$$

The coupling term J is usually positive, as shown by Eq. (22) (but see the discussion following Eq. (56)).

2.2 plasma-wave action equations

We describe the plasma waves following the dielectric operator approach of Cohen and Kaufman [15]. We ultimately treat the plasma waves in steady-state ($\partial_t = 0$) and the strong damping limit ($\partial_z = 0$), where the dielectric becomes an ordinary function. But this calculation reveals the validity of the latter approximation, and allows for extensions with advection or explicit time dependence.

Using the linearized Vlasov equation, the total charge-density fluctuation envelope $n_2 \equiv -n_{e2} + \sum_i Z_i n_{i2}$ experiences a ponderomotive drive n_{pnd} from the beating of modes 0 and 1:

$$\epsilon(\omega_2' + i\partial_t, k_2 - i\partial_z)n_2 = n_{\mathrm{pnd}}, \tag{12}$$

$$n_{\mathrm{pnd}} \equiv \frac{1}{2}\chi_e(\omega_2', k_2)\frac{c^2k_2^2}{\omega_{pe}^2}n_e a_0 a_1^*. \tag{13}$$

$\omega_2' \equiv \omega_2 - \vec{k}_2 \cdot \vec{u}$ is the Doppler-shifted plasma-wave frequency in the frame moving with the plasma flow $\vec{u}$ (ω_2 is in the lab frame). $\epsilon \equiv 1 + \chi$ is an operator, where the time and space derivatives reflect envelope evolution and $\chi \equiv \sum_j \chi_j$ is the total susceptibility. χ_e in n_{pnd} is taken simply as a function, as opposed to an operator. χ_j is the (linear) kinetic, collisionless susceptibility of species j (we assume all distributions are Maxwellian):

$$\chi_j \equiv -\frac{1}{2k_2^2\lambda_{Dj}^2}Z'(\zeta_j); \qquad \zeta_j \equiv \frac{\omega_2'}{k_2 v_{Tj}\sqrt{2}}. \tag{14}$$

$Z(\zeta) \equiv i\pi^{1/2}e^{-\zeta^2}\mathrm{erfc}(-i\zeta)$ is the plasma dispersion function [16], where erfc denotes the complimentary error function [17]. Gauss's law relates n_2 and n_{j2}:

$$n_{e2} = -(1 + \chi_I)n_2, \tag{15}$$

$$n_{i2} = -\chi_i\left(\frac{1}{Z_i} + \frac{m_e}{m_i}\frac{\epsilon}{\chi_e}\right)n_2 \tag{16}$$

$$\approx -\frac{\chi_i}{Z_i}n_2, \tag{17}$$

with $\chi_I \equiv \sum_i \chi_i$. For SRS, where the ion motion is negligible, we usually make the replacement $1 + \chi_I \to 1$ in the code to save computing time.

Expanding ϵ for slow envelope variation, and retaining only $\epsilon_r \equiv \mathrm{Re}\,\epsilon$ in the derivatives, gives

$$[\epsilon(\omega_2', k_2) + i\dot{\epsilon}\partial_t - i\epsilon'\partial_z]\, n_2 = n_{\mathrm{pnd}}. \tag{18}$$

$\dot\epsilon \equiv \partial\epsilon_r/\partial\omega_2'$ and $\epsilon' \equiv \partial\epsilon_r/\partial k_2$. Dividing by $i\dot\epsilon$, we find

$$[\partial_t + v_{g2}\partial_z + \nu_2 + i\delta\omega_2]\, n_2 = -i\frac{n_{\rm pnd}}{\dot\epsilon}. \tag{19}$$

$v_{g2} \equiv -\epsilon'/\dot\epsilon$ is the plasma-wave group velocity, $\nu_2 \equiv \mathrm{Im}[\epsilon]/\dot\epsilon$ is the collisionless damping rate, and $\delta\omega_2 \equiv -\epsilon_r/\dot\epsilon$ is the phase detuning. This makes contact with the usual envelope equation.

We now assume the plasma wave is in the strong damping limit, where its advection is neglected. This also implies that the instability is below its absolute threshold so that steady-state solutions are accessible. Quantitatively, this holds if $|v_{g2}\partial_z n_2| \ll |\nu_2 + i\delta\omega_2||n_2|$. The result is

$$[\partial_t + \nu_2 + i\delta\omega_2]\, n_2 = -i\frac{n_{\rm pnd}}{\dot\epsilon}. \tag{20}$$

In steady-state, this becomes a simple, local relationship between n_2 and $n_{\rm pnd}$:

$$\epsilon(\omega_2, k_2) n_2 = n_{\rm pnd}. \tag{21}$$

This follows directly from Eq. (12) by setting $\partial_t = \partial_z = 0$, but the more detailed derivation reveals the validity condition for the strong damping limit.

Replacing n_{e2} via Eqs. (15) and (21) yields a new form for the coupling term J, dependent only on the variables for modes 0 and 1:

$$J = \omega_0\tilde\Gamma_1 Z_0 Z_1. \tag{22}$$

The coupling coefficient $\tilde\Gamma_1$ is

$$\begin{aligned}
\tilde\Gamma_1 &\equiv \Gamma_S \mathrm{Im}\left[\frac{\chi_e}{\epsilon}(1+\chi_I)\right] &(23)\\
&= \frac{\Gamma_S g_\Gamma}{|\epsilon|^2}, &(24)\\
\Gamma_S &\equiv \frac{2\pi r_e}{m_e c^2}\frac{1}{\omega_0}\frac{k_2^2}{k_0|k_1|}, &(25)\\
g_\Gamma &\equiv |1+\chi_I|^2\mathrm{Im}\chi_e + |\chi_e|^2\mathrm{Im}\chi_I. &(26)
\end{aligned}$$

The second form of $\tilde\Gamma_1$ exhibits the resonance for $|\epsilon| \ll 1$. The over-tilde on $\tilde\Gamma_1$ indicates it will be modified below to account for beam focusing. $\tilde\Gamma_1$, and thus J, are usually positive. We now have a closed system for modes 0 and 1, with no independent equation for mode 2:

$$\begin{aligned}
\partial_t N_0 + \partial_z Z_0 &= -\omega_0\tilde\Gamma_1 Z_0 Z_1, &(27)\\
\partial_t N_1 - \partial_z Z_1 &= \omega_0\tilde\Gamma_1 Z_0 Z_1. &(28)
\end{aligned}$$

2.3 Steady-state equations for a spectrum of scattered waves

At this point we transition to steady state ($\partial_t = 0$) and work with intensities (although one can generalize what follows to include time evolution). Since we have assumed $\partial_z\omega_i = 0$, we multiply Eq. (27) by ω_0 and Eq. (28) by ω_1 to obtain

$$\begin{aligned}
d_z I_0 &= -\frac{\omega_0}{\omega_1}\tilde\Gamma_1 I_0 I_1, &(29)\\
-d_z I_1 &= \tilde\Gamma_1 I_0 I_1. &(30)
\end{aligned}$$

The bremsstrahlung source and TS which we will soon incorporate are expressed not in terms of intensity but spectral density $i_1(z,\omega_1)$, which is the intensity per angular frequency interval. The scattered intensity is then $I_1 = \int d\omega_1\, i_1$. We take the scattered-wave equation to apply independently at each ω_1, and integrate the coupling term in the pump equation, to find

$$\begin{aligned}
d_z I_0 &= -\int d\omega_1 \frac{\omega_0}{\omega_1}\tilde\Gamma_1 I_0 i_1, &(31)\\
-\partial_z i_1 &= \tilde\Gamma_1 I_0 i_1. &(32)
\end{aligned}$$

This is a totally incoherent treatment of the scattered light at different frequencies, and is unrealistic to the extent there is spectral “leakage” between nearby ω_1 intervals due to, e.g., envelope evolution.

2.4 Bremsstrahlung source and damping

We incorporate electron-ion inverse-bremsstrahlung light-wave damping (κ_0 and κ_1) phenomenologically for modes 0 and 1, as well as bremsstrahlung noise ($\tilde{\Sigma}_1$) for mode 1, to find

$$d_z I_0 = -\kappa_0 I_0 - \int d\omega_1 \frac{\omega_0}{\omega_1}\tilde{\Gamma}_1 I_0 i_1, \tag{33}$$

$$-\partial_z i_1 = -\kappa_1 i_1 + \tilde{\Sigma}_1 + \tilde{\Gamma}_1 I_0 i_1. \tag{34}$$

As for $\tilde{\Gamma}_1$, the over-tilde on $\tilde{\Sigma}_1$ denotes it will be modified due to focusing.

I_0 and i_1 represent integrals over solid angles in k space, which we now specify. Absolute solid angles are needed in the noise sources, and cannot be simply scaled away, because scattered intensities (relative to the pump strength) determine pump depletion. We follow closely Bekefi's book [18] in this section. We take $I_i = \Delta\Omega_i I_{i,\Omega}$ for $i = 0,1$ (see Secs. 1.6 and 1.7 of Bekefi). $I_{i,\Omega}$ is the intensity per solid angle interval $d\Omega$, which we assume is constant over the solid angle $\Delta\Omega_i$ that participates in the scattering. However, $\Delta\Omega_i$ varies with z according to $\Delta\Omega_i(z) = \Delta\Omega_i^v \eta_i(z)^{-2}$, where $\Delta\Omega_i^v$ is a constant "vacuum" solid angle. We set $\Delta\Omega_0^v = \Delta\Omega_1^v = \Omega_c$, where Ω_c is the solid angle of k_0 that falls in the beam's F cone. This is reasonable if the scattering mostly occurs in laser speckles that are near diffraction-limited. We relate Ω_c to the cone aperture half-angle θ_c and laser optics F-number F by

$$\Omega_c \equiv 2\pi(1-\cos\theta_c) \approx \frac{\pi}{4F^2}, \tag{35}$$

$$\cos\theta_c \equiv \left[1+\frac{1}{4F^2}\right]^{-1/2} \approx 1-\frac{1}{8F^2}. \tag{36}$$

The approximate forms apply for $F \gg 1$.

The upshot of the solid angle discussion (see especially Eq. (1.133) of Bekefi) is

$$\tilde{\Sigma}_1 = \Omega_c \eta_1^{-2} j(\omega_1), \tag{37}$$

where $j(\omega)$ is the emission coefficient j_ω of Bekefi, per $d\Omega$ and in one polarization. For j we use the results on p. 134 of Bekefi:

$$j(\omega_i) = \frac{\eta_i}{12\pi^3\sqrt{2\pi}}\frac{\omega_{pe}^4}{v_{Te}}\frac{m_e r_e}{c}\sum_{j\in\text{ions}}\frac{n_j}{n_e}Z_j^2 \ln\Lambda_{ej}. \tag{38}$$

$\ln\Lambda_{ej}$ is sometimes called the Gaunt factor and resembles the Coulomb logarithm, although it arises in calculations that do *not* impose ad hoc cutoffs on impact parameter integrals (see Chap. 3 of Bekefi). For the case $\omega_i > \omega_{pe}$, Bekefi finds $\Lambda_{ej} = v_{Te}/(\omega_i b_{\min})$ where

$$b_{\min} = \begin{cases} \frac{\gamma}{4}\frac{\hbar}{\sqrt{m_e T_e}} & \text{if } T_e > 77Z_j^2 \text{ eV}, \\ \left(\frac{\gamma}{2}\right)^{5/2} Z_j r_e \frac{m_e c^2}{T_e} & \text{otherwise.} \end{cases} \tag{39}$$

The first, high-T_e case typically applies for hohlraum conditions. The numerical pre-factors come from a detailed binary-collision calculation, and $\gamma = e^C \approx 1.781$ where $C \approx 0.577$ is the Euler-Mascheroni constant. Our expression for j does not include the enhanced emission for $\omega_i \approx \omega_{pe}$ due to collective effects [19], which may be important for modes with $n_{ci} \approx n_e$.

We find the absorption coefficient κ_i via Kirchoff's law (see Bekefi Sec. 2.3):

$$\kappa_i = \frac{j(\omega_i)}{\eta_i^2 B_v(\omega_i)}. \tag{40}$$

Our κ_i equals Bekefi's α_ω. B_v is the vacuum blackbody spectrum for one polarization, with units $dI/(d\omega\, d\Omega)$:

$$B_v(\omega) \equiv \frac{\hbar}{8\pi^3c^2}\frac{\omega^3}{e^{\hbar\omega/T_e}-1} \tag{41}$$

$$\approx \frac{\omega^2 T_e}{8\pi^3 c^2} \qquad \hbar\omega \ll T_e. \tag{42}$$

j given above was found for collision durations short compared to the light-wave period, which entails the Jeans limit $\hbar\omega \ll T_e$. We therefore use the approximate form of B_v to obtain

$$\kappa_i = \frac{\sqrt{2}}{3\sqrt{\pi}}\frac{r_e c}{\eta_i\omega_i^2}\frac{\omega_{pe}^4}{v_{Te}^3}\sum_{j\in\text{ions}}\frac{n_j}{n_e}Z_j^2\ln\Lambda_{ej}. \tag{43}$$

We only include bremsstrahlung when the plasma is under-dense ($\omega_i > \omega_{pe}$) for a given frequency; in the opposite case, we set $\kappa_i = \tilde{\Sigma}_1 = 0$.

For an optically thick plasma ($\partial_z i_1 = 0$), and in the absence of the pump ($I_0 = 0$), we obtain for i_1 from Eq. (34) the optically-thick fluctuation level i_1^{OT}:

$$i_1^{\mathrm{OT}} \equiv \frac{\Sigma_1}{\kappa_1} = \frac{\Omega_c}{f}B_v(\omega_1). \tag{44}$$

We thus recover the familiar blackbody spectrum, required by Kirchoff's law. The common factor η_1^2 that usually appears in the blackbody spectrum in a plasma is absent due to our treatment of solid angles. f is defined in Sec. 2.6.

2.5 Thomson scattering

Thomson scattering (TS) refers to scattering off plasma-wave fluctuations resulting from particle discreteness ([20], p. 308). Had we retained a separate plasma wave equation, the fluctuations would appear in it via Čerenkov emission [6]. It is an important noise source for backscatter, especially for SBS. We utilize the form factor S from Eq. (138) of Ref. [20], valid for arbitrary (non-Maxwellian) distributions, generalized to multiple ion species:

$$(2\pi)^{-1}|\epsilon|^2 S(\vec{k},\omega) = |1+\chi_I|^2 F_e + |\chi_e|^2 \sum_{j\in\text{ions}} \frac{n_j}{n_e} Z_j^2 F_j \tag{45}$$

$$F_j \equiv \int d^3v\ f_j(\vec{v})\delta(\omega+\vec{k}\cdot\vec{v}). \tag{46}$$

f_j is the distribution function of species j normalized so that $\int d^3v\ f_j = 1$. For a Maxwellian,

$$F_j = \frac{1}{kv_{Tj}\sqrt{2\pi}} e^{-\zeta_j^2} = \frac{(k\lambda_{Dj})^2}{\pi\omega}\mathrm{Im}\chi_j, \tag{47}$$

and

$$\frac{\omega|\epsilon|^2}{2(k\lambda_{De})^2} S = g_\tau \equiv |1+\chi_I|^2 \mathrm{Im}\chi_e + |\chi_e|^2 \sum_{j\in\text{ions}} \frac{T_j}{T_e}\mathrm{Im}\chi_i. \tag{48}$$

This form agrees with the multiple-ion result in Eq. (3) of Ref. [21].

Since TS transfers energy between the pump and scattered waves, we include it in both equations:

$$d_z I_0 = -\kappa_0 I_0 - \int d\omega_1 \frac{\omega_0}{\omega_1} I_0(\tau_1 + \tilde{\Gamma}_1 i_1), \tag{49}$$

$$-\partial_z i_1 = -\kappa_1 Z_1 + \tilde{\Sigma}_1 + I_0(\tau_1 + \tilde{\Gamma}_1 i_1). \tag{50}$$

The Thomson cross-section is contained in τ_1, which for a Maxwellian plasma is:

$$\tau_1 \equiv \frac{\Omega_c}{2\pi} n_e r_e^2 \psi S(k_2,\omega_2') = \frac{\tau_S g_\tau}{|\epsilon|^2}, \tag{51}$$

$$\tau_S \equiv \frac{\Omega_c\psi}{4\pi^2}\frac{r_e T_e}{m_e c^2}\frac{k_2^2}{\omega_2'}. \tag{52}$$

$\psi \equiv 1-\sin^2\theta_s\sin^2\theta_p$. θ_s is the angle between $\vec{k}_0$ and $\vec{R}$, the vector from source to "observation point". For a beam with large F, most of the backscatter occurs near the beam axis, and $\theta_s \sim \theta_c \ll 1$ (for large F). θ_p is the difference between the azimuthal angles (in the plane normal to $\vec{k}_0$) of $\vec{A}_0$ and $\vec{R}$, which for a cylindrically symmetric beam and linearly polarized pump varies uniformly over 2π. We take $\psi = 1$, which may somewhat overstate the actual Thomson level.

It is useful to note that $i_\tau \equiv \tau_1/\Gamma_1$ sometimes plays the role of an effective seed level for i_1:

$$i_\tau \equiv \frac{\tau_1}{\Gamma_1} = \frac{\tau_S g_\tau}{\Gamma_S g_\Gamma}. \tag{53}$$

For the special case $T_i = T_e$, we have $g_\tau = g_\Gamma$ and i_τ is independent of χ_j:

$$i_\tau = \frac{\tau_S}{\Gamma_S} = \frac{\Omega_c\psi}{(2\pi)^3}\frac{\omega_0}{\omega_2'}T_e k_0|k_1|, \qquad T_i = T_e. \tag{54}$$

This fact is used in Sec. 5 to discuss the relation of TS to linear gain.

2.6 Whole-beam focusing

We wish to incorporate the effects of whole-beam focusing in a simple way. The equations as written hold locally in z, but do not model focusing. To do this, we treat the transverse intensity patterns of I_0 and I_1 to be uniform flattops of varying area $A(z)$. The beam focuses at the focal spot z_F, where A attains its minimum $A(z_F)$. Let $\tilde{I}_i \equiv I_i(z)/f(z)$ be the total power at z divided by the focal spot area, with focusing factor $f \equiv A(z_F)/A(z) \le 1$. Substituting $(I_0, i_1) = f\cdot(\tilde{I}_0,\tilde{i}_1)$ into Eqs. (49-50), and freely commuting f with ∂_z, yields the principal equations solved by DEPLETE:

$$d_z I_0(z) = -\kappa_0 I_0 - I_0 \int d\omega_1 \frac{\omega_0}{\omega_1}(\tau_1 + \Gamma_1 i_1), \tag{55}$$

$$\partial_z i_1(z,\omega_1) = \kappa_1 i_1 - \Sigma_1 - I_0(\tau_1 + \Gamma_1 i_1). \tag{56}$$

The untilded coefficients are

$$\Gamma_1 \equiv f\tilde{\Gamma}_1 \qquad \Sigma_1 \equiv f^{-1}\tilde{\Sigma}_1. \tag{57}$$

In Eqs. (55-56) and henceforth, all I_i and i_1 are understood to have suppressed over-tildes, that is, refer to total transverse powers over focal-spot area. Similarly, the plasma-wave amplitude from Eq. (21) can be written

$$\frac{n_2}{n_e} = \frac{1}{2}\frac{\chi_e}{\epsilon}\left[\frac{ck_2}{\omega_{pe}}\right]^2 f\ \tilde{a}_0\tilde{a}_1^* \tag{58}$$

with $\tilde{a}_i \equiv \tilde{I}_i\lambda_i^2/(P_{em}\eta_i)$; see Eq. (8).

All symbols in Eqs. (55-56) are positive, with one possible exception. Γ_1 may be negative for SBS in case the Doppler-shifted plasma-wave frequency, ω_2', is negative. This corresponds to the scattered wave having a higher frequency than the pump, in the plasma frame. The scattered wave then gives energy to the pump, and DEPLETE handles this situation correctly.

3 Numerical method

We wish to solve Eqs. (55-56) from the laser entrance ($z = 0$) to the end of the ray ($z = L_z$). For backscatter (considered in this paper), we give I_{0L} and $i_{1R}(\omega_1)$ as boundary conditions, where $f_L \equiv f(z = 0)$ and $f_R \equiv f(z = L_z)$. We solve this two-point boundary value problem via a shooting method, marching from right to left. We guess I_{0R} and solve the initial value problem from $z = L_z$ down to $z = 0$, and iterate until the resulting I_{0L} is sufficiently close to the desired value. Because I_{0R} is just one scalar, it is more feasible to shoot on it than on the set of values $i_{1L}(\omega_1)$. Generalizing our approach to 3D, where one would have to shoot on $I_{0R}(x, y)$ over a transverse plane, is much more difficult; a different technique for 3D pump depletion is used in the code SLIP [22]. For the right-boundary seed value i_{1R}, we either use 0 or the optically-thick i_1^{OT} from Eq. (44). The choice seems to have little effect, since volume sources (either TS or bremsstrahlung) typically produce a comparable (or larger) noise level after a short distance.

We solve the governing equations, Eqs. (55-56) by operator splitting [23, 24]. Let the operator B solve the "bremsstrahlung" system

$$d_z I_0 = -\kappa_0 I_0, \tag{59}$$

$$\partial_z i_1 = \kappa_1 i_1 - \Sigma_1, \tag{60}$$

and the operator C solve the "coupling-Thomson" system

$$d_z I_0 = -I_0 \int d\omega_1 \frac{\omega_0}{\omega_1}(\tau_1 + \Gamma_1 i_1), \tag{61}$$

$$\partial_z i_1 = -I_0(\tau_1 + \Gamma_1 i_1). \tag{62}$$

To advance the solution from the discrete gridpoint z^n down to z^{n-1} (the decreasing index matches DEPLETE's right-to-left marching), we first apply B for a half-step, then C for a full step, then B for a half-step again. The splitting theorem guarantees that, as long as B and C are second-order accurate operators, then the overall step is second-order accurate as well. Schematically, a complete step is

$$\{I_0, i_1\}^{n-1} = B_{1/2}C_1B_{1/2}\{I_0, i_1\}^n. \tag{63}$$

A main application of DEPLETE is to plasma profiles generated by hydrodynamic simulations. Typically, we are given plasma conditions like density and temperature along a 1D ray path for a set of z values. The z-dependent coefficients in the governing equations are therefore known only at prescribed points $\{z^n\}$. We use linear interpolation to find the coefficients at the needed intermediate points, as shown below. We stress that the numerical accuracy of DEPLETE is strongly influenced by the quality of the given plasma conditions.

3.1 The bremsstrahlung step B

B must solve Eqs. (59-60) with κ_i and Σ_1 constant, to at least second-order accuracy. This linear system is readily solved analytically. Since there are two "half-steps" of B in Eq. (63), we consider a generic step of size Δz with initial conditions $\{I_0, i_1\}^1$, yielding new values $\{I_0, i_1\}^0$. $X^{1/2} = (X^0 + X^1)/2$ denotes the zone-centered value of some quantity X. If $\kappa_1^{1/2} \neq 0$, we find

$$I_0^0 = I_0^1 \exp[\kappa_0^{1/2} \Delta z], \tag{64}$$
$$i_1^0 = (i_1^1 - i_1^{\mathrm{OT},1/2}) \exp[\kappa_1^{1/2} \Delta z] + i_1^{\mathrm{OT},1/2}. \tag{65}$$

Eq. (65) applies separately at each ω_1. For the special case $\kappa_1^{1/2} = 0$, Eq. (65) is replaced with

$$i_1^0 = i_1^1 + \Sigma_1^{1/2} \Delta z \qquad (\kappa^{1/2} = 0). \tag{66}$$

The rightmost B in Eq. (63) advances the system from z^n to $z^{n-1/2}$. Accordingly, for this step, the needed coefficients in Eqs. (64-66) are interpolated at 1/4 the way from z^n to z^{n-1}: $X^{1/2} = [(1/4)X^{n-1} + (3/4)X^n]$. Similarly, the leftmost B in Eq. (63) advances the system from $z^{n-1/2}$ to z^{n-1} and uses $X^{1/2} = [(3/4)X^{n-1} + (1/4)X^n]$. In both cases $\Delta z = (z^n - z^{n-1})/2$.

3.2 The coupling-Thomson step C

We now turn to the C operator. I_0 is evolved via a conservation law of the C system, Eqs. (61-62), namely

$$d_z \left[I_0 - \int d\omega_1 \, \frac{\omega_0}{\omega_1} i_1 \right] = 0. \tag{67}$$

On the discrete z grid, this gives

$$I_0^{n-1} = I_0^n + \int d\omega_1 \, \frac{\omega_0}{\omega_1} (i_1^{n-1} - i_1^n). \tag{68}$$

Before doing this, we must advance i_1 using Eq. (62) with constant $I_0 = I_0^n$ (that is, we neglect pump depletion within a zone). This gives rise to a numerical challenge. Namely, the coefficients τ_1 and Γ_1 are both proportional to $|\epsilon|^{-2}$, and contain a narrow resonance where $\mathrm{Re}\,\epsilon = 0$ if $\mathrm{Im}\,\epsilon$ is small (that is, where the beating of the light waves drives a natural plasma wave). Integrating through these sharp peaks with a standard ODE method like Runge-Kutta performs very poorly unless the resonance is well-resolved by the z grid (which it usually is not on the z grids from hydrodynamic codes). To alleviate this problem, the key observation is that ϵ itself varies slowly in space, even though $|\epsilon|^{-2}$ varies rapidly near resonance. We can therefore represent ϵ as linearly varying with z across a cell, and analytically solve the resulting system. We merely quote the result here, and refer the reader to Appendix B for the derivation and definition of the relevant quantities:

$$i_1^{n-1} = (i_1^n + i_\tau) e^{B_\Gamma \Delta w_n} - i_\tau. \tag{69}$$

4 Benchmark on linear profiles

This section compares the results of DEPLETE with those of NEWLIP and pF3D on two contrived profiles with weak linear gradients, one for SRS and another for SBS. DEPLETE and pF3D embody quite different physical models, each with their own approximations and limitations. One can view their favorable comparison here as a "cross-validation" of these models in a regime where they should agree.

To compare with the NEWLIP linear gain G_l (see Appendix A), we need a noise level against which to compare the DEPLETE scattered spectrum at the laser entrance, i_{1L}. For this noise level we choose i_1^{br} at $z = 0$, given by solving Eq. (56) with just the bremsstrahlung terms and in the absence of the pump laser ($I_0 \to 0$):

$$\partial_z i_1^{br} = \kappa_1 i_1^{br} - \Sigma_1. \tag{70}$$

Note this is exactly Eq. (60). We then introduce the DEPLETE gain G_d:

$$G_d \equiv \ln \frac{i_{1L}}{i_{1L}^{br}} = \frac{\text{“scattering”}}{\text{“noise”}}, \tag{71}$$

where i_{1L} is the solution to the full DEPLETE equations. G_l and G_d are exactly equal under the following conditions: there is no pump depletion, no TS ($\tau_1 = 0$), no absorption of scattered light ($\kappa_1 = 0$), and no volume bremsstrahlung noise ($\Sigma_1 = 0$); the only seeding in DEPLETE is then via the boundary values $i_{1R}(\omega_1)$.

4.1 SRS benchmark

The spatial profiles of our SRS benchmark plasma conditions are shown in Fig. 1. We use a profile length $L_z = 510\lambda_0$, pump vacuum wavelength $\lambda_0 = (1054/3)$ nm, fully-ionized H ions with $T_i = 1$ keV, and no plasma flow ($\vec{u} = 0$). In both the DEPLETE and pF3D runs of this section, SBS was not included. Fig. 2 plots the resulting reflectivities for several pump strengths. Although these are all above the homogeneous absolute instability threshold of $I_0^{ab} \approx 0.21$ PW/cm^2, the time-dependent pF3D runs rapidly approach a steady state and show no signs of a temporally-growing mode [1]. The weak gradients, or incoherent noise source, may lead to stabilization. After increasing exponentially with I_{0L} for weak pumps, the reflectivity rolls over. This saturation due to pump depletion is generic for three-wave interactions in the strong damping limit, as demonstrated analytically by Tang [25].

We compare the gains G_l and G_d from NEWLIP and DEPLETE, for several pump strengths, in Fig. 3. The general shapes of the gains are quite close, although their absolute levels differ. For the weakest pump strength, where pump depletion plays little role (as can be inferred from the reflectivity plot in Fig. 2), the peak G_d is slightly higher than G_l. This is due to the volume sources in DEPLETE, namely TS and bremsstrahlung noise. To illustrate this, we plot G_d found with no Thomson scattering ($\tau_1 = 0$) as the black dotted curve. It is intermediate between the two other curves near the peak, and overlaps G_l away from the peak. The curves for the two larger values of I_{0L} in Fig. 3 show G_d to be progressively farther below G_l at peak. This results from pump depletion, which the reflectivity plot clearly shows is significant for $I_{0L} \gtrsim 0.8$ PW/cm^2. The bremsstrahlung noise level i_1^{br} varies between (2.4-4.1)$\times10^{-9}$ W/cm^2/(rad/sec) over $\lambda_1 = 650$ to 550 nm.

We also compared DEPLETE to the massively-parallel, paraxial laser propagation code pF3D [26]. This code solves for the slowly-varying envelopes of the pump laser, nearly-backscattered SRS and SBS light

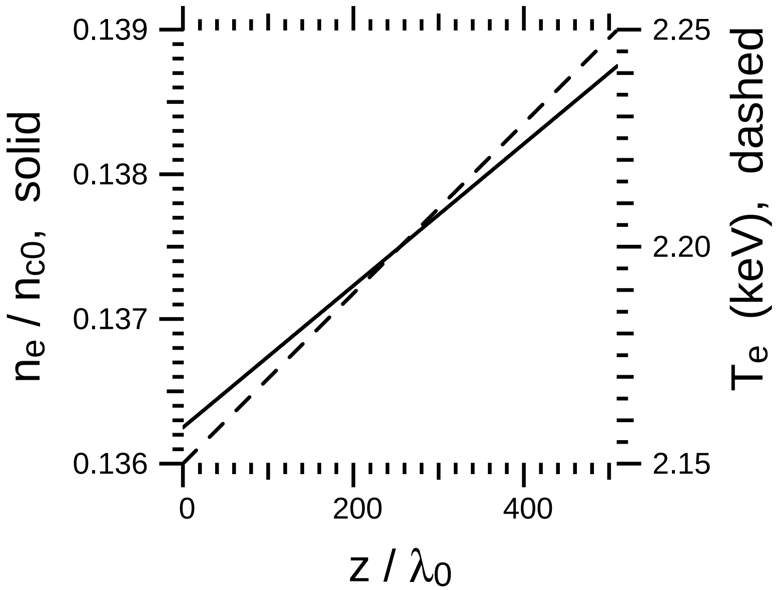

Figure 1: Plasma conditions for SRS benchmark.

waves, and the daughter plasma waves, in space and time. A carrier ω^{en} is chosen for each mode (except for the ion acoustic wave), and the corresponding rapid time variations are averaged over. A local eikonal k^{en}, given by the appropriate ω^{en} and dispersion relation with local plasma conditions, contains the rapid space variation. Kinetic quantities, such as Landau damping rates and Thomson cross-sections, are variously found from (linear) kinetic formulas or fluid approximations. There is no bremsstrahlung source, but the pump and scattered light waves all experience inverse-bremsstrahlung damping. The plasma waves undergo Landau damping, and the advection term $v_{g2}\partial_x n_2$ is retained (i.e., they are not treated in the strong damping limit). The noise source in pF3D is plasma-wave fluctuations chosen to produce the correct TS level, and uniformly distributed over a square in $k_\perp$ space (corresponding to the transverse x and y directions) extending to half the Nyquist k in both k_x and k_y.

To replicate the 1D model of DEPLETE, we performed "plane-wave" simulations in pF3D. The incident laser at the $z = 0$ entrance plane is uniform in the x and y directions (i.e., there is no structure like speckles), both of which are periodic with size $L_x = L_y = 128\lambda_0$ and

[1] The homogeneous absolute instability threshold I_0^{ab} is such that the undamped amplitude growth rate $\gamma_0(I_0^{ab})$ satisfies $\gamma_0 = (1/4)|v_{g1}v_{g2}|^{1/2}(\kappa_1 + \kappa_2)$ where $\kappa_2 \equiv 2\nu_2/v_{g2}$ is the plasma-wave spatial energy damping rate.

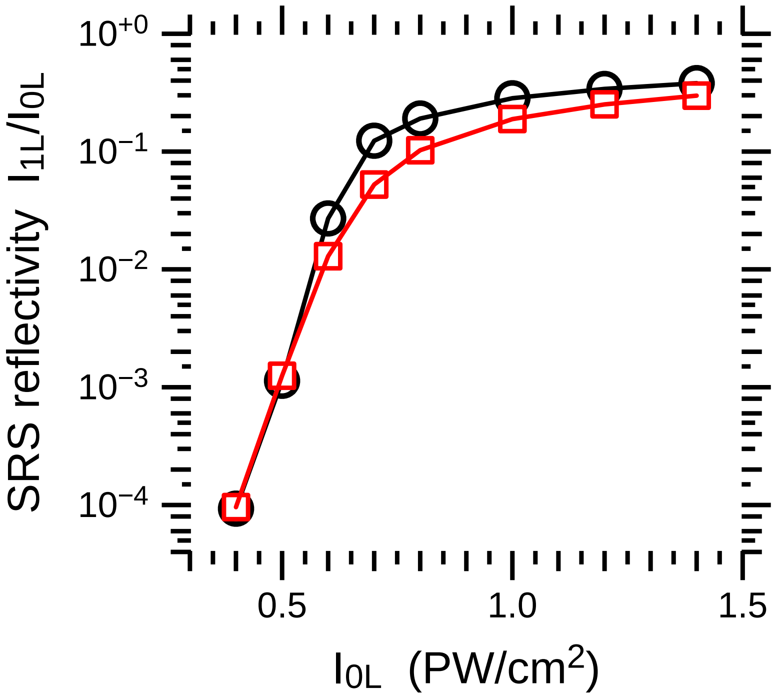

Figure 2: (Color online.) SRS reflectivity vs. pump intensity for the SRS benchmark profile of Fig. 1. The black circles and red squares are for pF3D and DEPLETE, respectively.

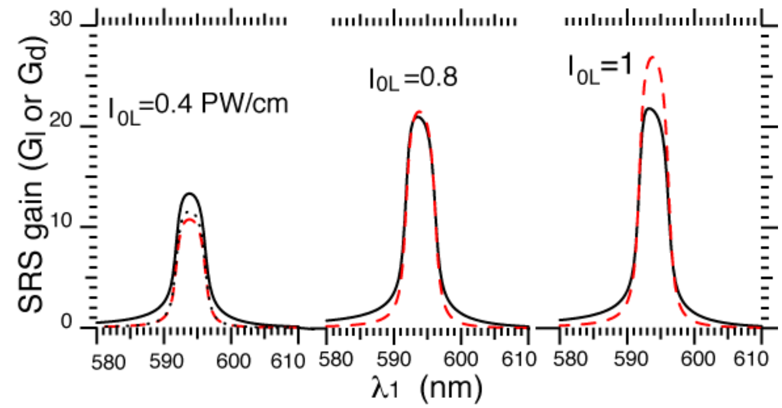

Figure 3: (Color online.) DEPLETE gain G_d (black solid), NEWLIP gain G_l (red dashed), and G_d with no TS for $I_{0L} = 0.4$ PW/cm^2 ($\tau_1 = 0$, black dots), for SRS benchmark. Thomson scattering and volume bremsstrahlung noise enhance G_d over G_l for the smallest I_{0L}, while pump depletion suppresses G_d for the larger two.

grid spacing $dx = dy = 1.33\lambda_0$. The z spacing is $dz = 2\lambda_0$. As described above, the TS noise fills a square in $k_\perp$ space extending to $k_x, k_y = \pm k_{1n}$, with $k_{1n} = (3/16)k_{0v}$ and $k_{0v} \equiv \omega_0/c$. We enveloped the SRS backscattered light around $\omega_1^{en} = 0.592\omega_0$ (λ_1=593.3 nm), which has the highest linear gain. Over the slight variation of our profile, the average $k_1^{en} = 0.461k_{0v}$.

DEPLETE requires a solid angle Ω_c, which we express in terms of an F-number F, for TS (as well as bremsstrahlung emission, which we did not include in the pF3D comparisons). Taking k_1^{en} and k_{1n} to determine the focal length and spot radius, one finds $F = k_1^{en}/2k_{1n} = 1.23$. The scattered light does not uniformly fill the noise square in $k_\perp$ space, but rather develops into a somewhat hollow "ring" with a radius $\approx 0.12k_{0v}$ (departing more from a square for stronger pumps); there is some ambiguity in the appropriate F to use. We choose $F = 1$, which leads to very close reflectivities for the weakest-pump case shown in Fig. 2, and is near the noise-square estimate $F = 1.23$. Sidescatter at these angles may stress the accuracy of pF3D's paraxial approximation.

Figure 2 shows the DEPLETE and pF3D SRS reflectivities for the benchmark profile. The pF3D values are taken at t =39.4 ps, after which time all reflectivities remain roughly constant (the laser ramped from zero to full strength over 10 ps). The agreement is quite good, especially in the linear (weak pump) and the strongly-depleted (strong pump) regimes. This increases confidence in the validity of the different approximations made in both codes. It took about 2 secs of wall time for DEPLETE to run on one Itanium CPU, as opposed to 5300 secs on 16 of these CPUs for pF3D to advance 10 ps.

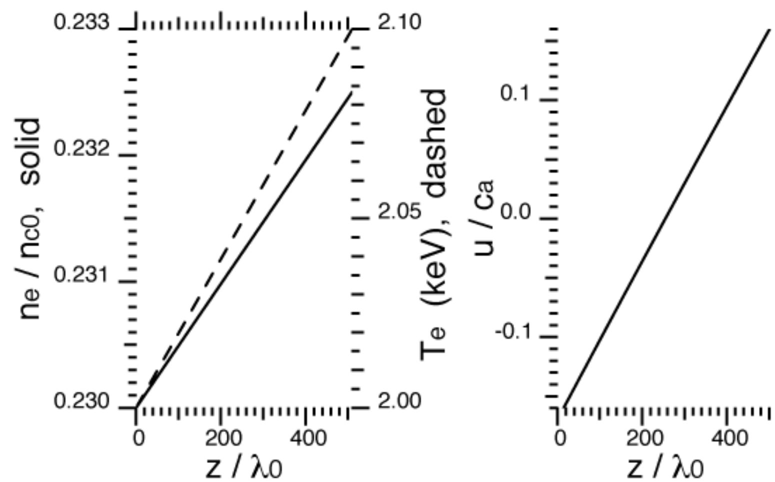

Figure 4: SBS benchmark profile.

4.2 SBS benchmark

We performed an SBS benchmark (with SRS neglected) using the profiles in Fig. 4. The ions were fully-ionized He ($Z = 2$, $A = 4$) with $T_i = T_e/5$. The parallel flow velocity u is shown normalized to the local acoustic speed $c_a^2 \equiv (ZT_e + 3T_i)/Am_p$. The pump wavelength and profile length match the SRS benchmark. The SBS reflectivity vs. pump strength is plotted in Fig. 5, which shows pump depletion for $I_{0L} \gtrsim 1.25$ PW/cm^2. We estimate the absolute threshold $I_0^{ab} = 2.6$ PW/cm^2 and stay below this. We used $F = 1.7$ since this gives good agreement with pF3D "plane-wave" simulations for low I_0. However, for larger values of I_0 a ring in $k_\perp$ space develops, similar to the SRS runs, and is accompanied by a large increase in reflectivity.

Figure 6 compares the DEPLETE and NEWLIP gains, G_d and G_l. For the smaller two pumps we see the enhancement of G_d over G_l due to TS (even though pump depletion has set in for the second case $I_{0L} = 1.4$ PW/cm^2), as discussed in Sec. 5. The dotted black curve for $I_{0L} = 0.6$ PW/cm^2 is G_d computed with no TS, and shows the modest increase in G_d stemming from bremsstrahlung volume (as opposed to boundary) noise. The elevated plateau of G_d to the left of the peak is also due to TS. I_{0L} =2.5 PW/cm^2 gives $G_d < G_l$ due to strong pump depletion. In all cases the wavelength and width of the main peak of the two spectra are similar. i_1^{br}, the bremsstrahlung solution, varies slightly from (4.17-4.25)$\times 10^{-9}$ W/cm^2/(rad/sec) over $\lambda_1 - \lambda_0 = 20$ to -3 Å.

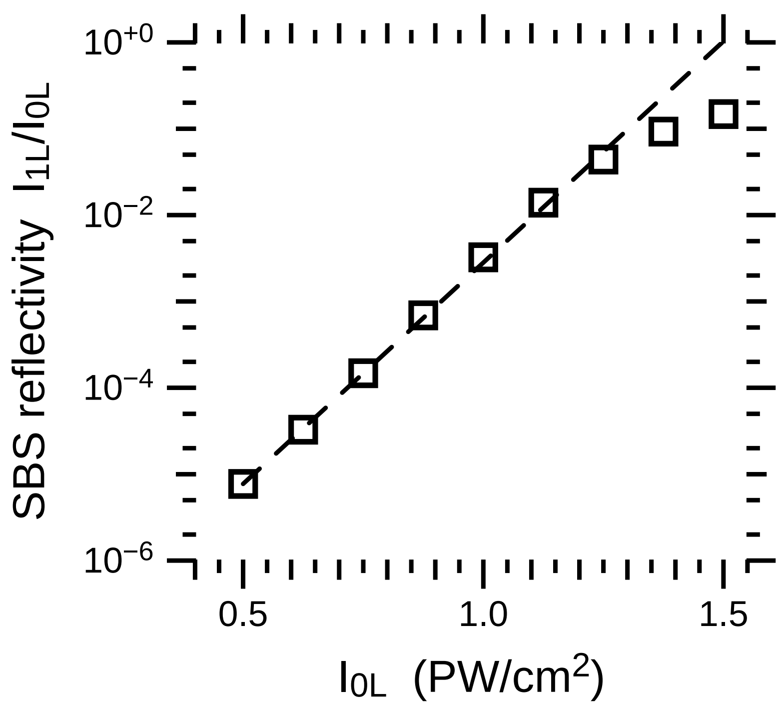

Figure 5: SBS reflectivity for SBS benchmark profile. The squares are DEPLETE results, and the dashed line is an extension of the low-I_{0L} results.

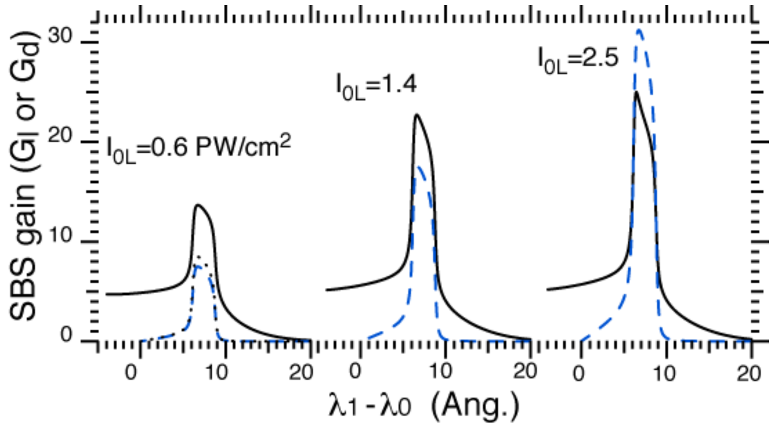

Figure 6: (Color online.) SBS DEPLETE gain G_d (black solid), NEWLIP gain G_l (blue dashed), and G_d without TS for I_{0L} =0.6 PW/cm^2 ($\tau_1 = 0$, black dotted), for SBS benchmark profile.

5 The relation of Thomson scattering to linear gain

As seen in our benchmark runs, TS leads to an enhancement of the DEPLETE gain compared to the NEWLIP gain (for negligible pump depletion). This is readily seen via the scattered-wave equation with just coupling and TS, Eq. (62):

$$\partial_z i_1 = -I_0(\tau_1 + \Gamma_1 i_1). \tag{72}$$

We use Eq. (53) to obtain

$$\partial_z i_1 = -\gamma(i_\tau + i_1). \tag{73}$$

$\gamma \equiv I_0\Gamma_1$ is the spatial gain rate. Typically, γ has a narrow peak in z at the resonance point, while i_τ varies slowly. For simplicity, we hold i_τ constant at the resonance point, and solve for i_1 across the region $z = 0$ to L_z which includes the resonance. In our usual notation,

$$i_{1L} = (i_{1R} + i_\tau)e^{G_l} - i_\tau. \tag{74}$$

$G_l \equiv \int_0^{L_z} dz\, \gamma$ is the NEWLIP linear gain. For $G_l \ll 1$, $i_{1L} = i_{1R}(1 + G) + i_\tau G$, and emission due to the boundary source dominates over TS. In the opposite limit,

$$i_{1L} = (i_{1R} + i_\tau)e^{G_l}, \qquad e^{G_l} \gg 1. \tag{75}$$

TS therefore gives rise to an effective boundary source i_τ (for a narrow resonance). In this sense, it does not significantly alter the shape of the gain spectrum (i_τ varies slowly with ω_1). However, it *does* lead to a difference in the absolute magnitude of the scattered spectrum, as embodied in an "absolutely-calibrated" gain like the DEPLETE gain G_d (where the bremsstrahlung emission is used as the noise level). As an illustration, let us take $i_{1R} = i_1^{\mathrm{OT}}$, the optically-thick bremsstrahlung result of Eq. (44), for simplicity evaluated at the resonance point in the Jeans limit $\hbar\omega_1 \ll T_e$. Moreover, we set $T_i = T_e$ so that i_τ assumes the simple form of Eq. (54). The effective seed is then

$$i_{1R} + i_\tau \to i_1^{\mathrm{OT}}\left(1 + f\eta_0\eta_1\frac{\omega_0^2}{\omega_1\omega_2'}\right). \tag{76}$$

The second term on the right ($= i_\tau/i_1^{\mathrm{OT}}$) is typically $\lesssim 10$ for SRS: for our SRS benchmark, $i_\tau/i_1^{\mathrm{OT}} \approx 3$. But, it can be quite large for SBS since $\omega_0 \gg \omega_2'$ (for our SBS benchmark, $i_\tau/i_1^{\mathrm{OT}} \approx 400$). A similar result is found in Ref. [6]. The authors explain this on the thermodynamic ground that bremsstrahlung and Čerenkov emission (which produces TS) generate equal light- and plasma-wave action, so the light-wave energy dominates by the frequency ratio. This manifests itself in the ω_0/ω_2' ratio in Eq. (76), which is much larger for SBS.

6 Simulation of SBS experiments

Experiments have been conducted recently at the Omega laser to study LPI in conditions similar to those anticipated at NIF[27]. These shots use a gas-filled hohlraum, and a set of "heater" beams to pre-form the plasma environment. An "interaction" beam is propagated down the hohlraum axis after being focused through a continuous phase plate (CPP)[28] with an f/6.7 lens to a vacuum best focus of 150 μm. The plasma conditions along the interaction beam path have been measured using Thomson scattering [29] validating 2-dimensional HYDRA [30] hydrodynamic simulations that show, 700 ps after the rise of the heater beams, a uniform 1.5-mm plasma with an electron temperature of $\approx$2.7 keV [31].

Figure 7(a) displays the instantaneous SBS reflectivity increasing exponentially with the interaction beam intensity 700 ps after the rise of the heater beams. These experiments employed a 1 atmosphere gas-fill with 30% CH_4 and 70% C_3H_8 to produce an electron density along the interaction beam path of $0.06n_{c0}$. Three-dimensional pF3D simulations agree well with the experiments [32]. Unlike the plane-wave simulations discussed in Sec. 4.1, these simulations include the full speckle physics. The DEPLETE results (blue solid curve) fall well below the experimental data in the regime where pump depletion does not play a significant role ($I_0 \lesssim 2$ PW/cm^2). This indicates that speckles are enhancing the SBS.

To put an upper bound on the speckle enhancement, we consider how much the coupling increases for the completely phase-conjugated mode [33]. This mode has a transverse intensity pattern perfectly correlated with that of the pump, and therefore enhances the coupling coefficient Γ_1 [34]. For an RPP-smoothed beam with intensity distribution $\sim e^{-I/I_c}$, this effectively doubles Γ_1. The blue dashed curve in Fig. 7 shows the DEPLETE results with twice the nominal coupling. The two DEPLETE curves bracket the experimental reflectivities. The threshold intensity for which SBS equals 5% is 1.8 PW/cm^2 and 0.9 PW/cm^2 for DEPLETE with the nominal and twice-nominal coupling, respectively. The experimental threshold is about 1.5 PW/cm^2.

Comparison of DEPLETE and pF3D is displayed in Fig. 7(b). These calculations were performed using plasma conditions from a HYDRA simulation, for a configuration similar to that of Fig. 7(a), but with a higher heater-beam energy. The resulting conditions are similar, except the electron temperature is higher (about 3.3 keV). The DEPLETE reflectivity with the nominal coupling (solid blue curve) lies below the pF3D results for the two intermediate values of I_0. This demonstrates speckle effects enhance the pF3D reflectivity. The DEPLETE results for $2\times\Gamma_1$ (dashed blue curve) brackets the pF3D results before strong pump depletion occurs, as for the experimental data. Preliminary analyses have been done with DEPLETE and pF3D for a series of Omega experiments designed to study the role of ion Landau damping on SBS [11]. These also show a significant enhancement due to speckles, which are bracketed by DEPLETE with the $2\times\Gamma_1$ method just described.

7 Analysis of NIF ignition design

In this section, we exercise DEPLETE on an actual NIF indirect-drive ignition target design. The target was designed using the hydrodynamic code LASNEX [35]. For more details about the design see Ref. [36]; LPI analysis for this and similar ignition targets, including massively-parallel, 3D pF3D simulations, can be found in Ref. [37]. The design utilizes all 192 NIF beams (at 351 nm "blue" light), which deliver 1.3 MJ of laser energy. We analyze LPI along the 30° cone of beams (one of the two "inner" cones). The pulse shape for one quad (a bundle of four beams), expressed as nominal intensity at best focus, is shown in Fig. 8, and reaches a maximum of 0.33 PW/cm^2. The speckle pattern for a quad approximately corresponds to an F-number of $F = 8$, which we use for DEPLETE's noise sources (but each beam individually has $F = 20$ optics). The focal spot is elliptical with semi-axis lengths of 693, 968 μm. The peak temperature of the radiation drive is 285 eV. The materials are as follows: the capsule ablator is Be, a plastic (CH) liner surrounds the laser entrance hole, the hohlraum wall is Au-U with a thin outer layer of 80% Au-20% B (atomic ratio), and the initial fill gas is 80% H-20% He. The lower-Z components are included in the last two mixtures to reduce SBS by increasing the ion Landau damping of the acoustic wave.

We performed DEPLETE calculations, with both SRS and SBS, at several times and over 381 ray paths for each time. Ray-based analysis of target designs, namely by computing NEWLIP gains G_l, is a routine first assessment of LPI risk at LLNL. At each time, a set of ray paths are traced using randomized initial conditions within each cone, and accounting for refraction. Plasma conditions and laser intensity are then found along these refracted rays. We run DEPLETE on each ray separately, using the initial intensity at a point chosen at a suitably low density. This yields a spectrum of reflected light, and a pump intensity, versus distance along the ray.

We now must take an appropriate "average" over the rays to characterize the LPI on a cone. Regarding NEWLIP gains, this has led

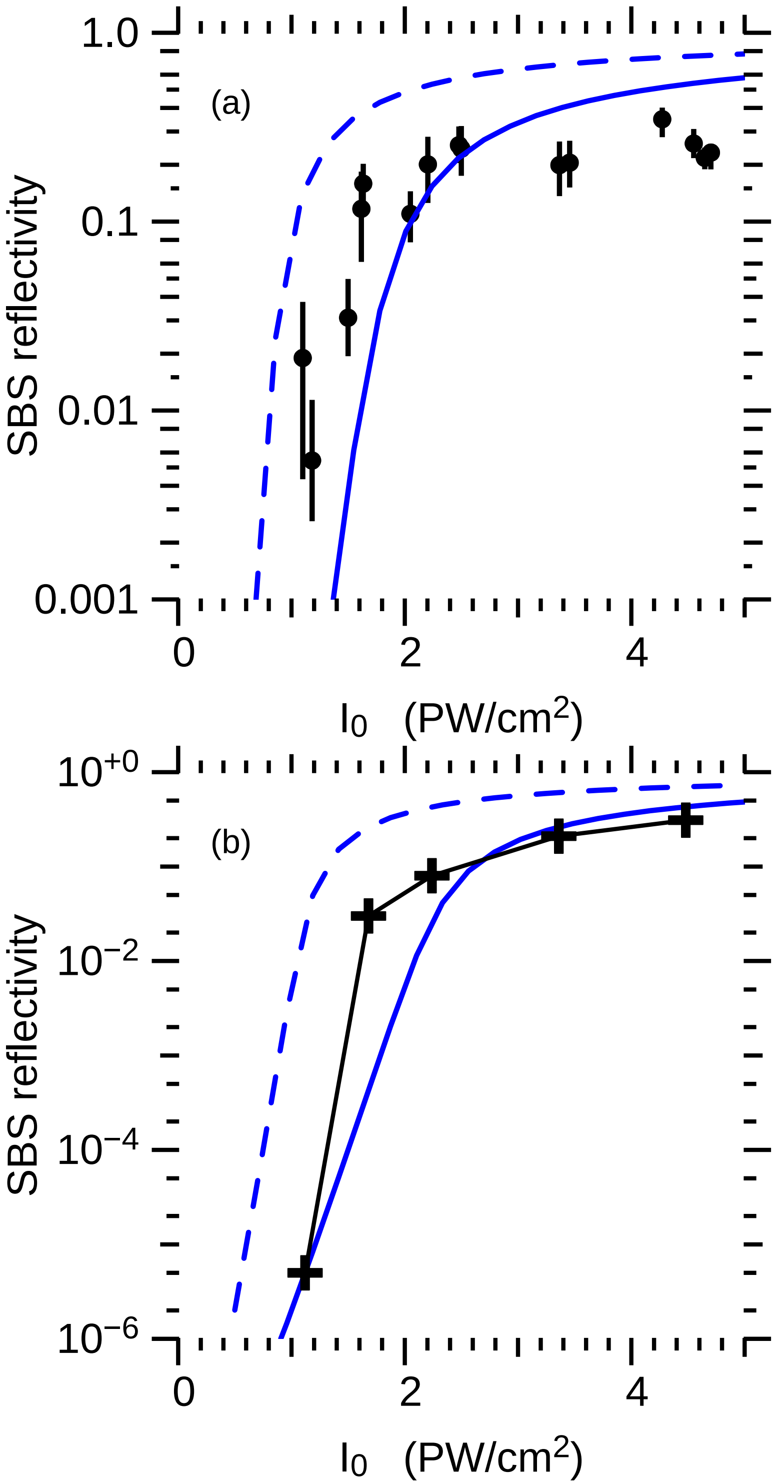

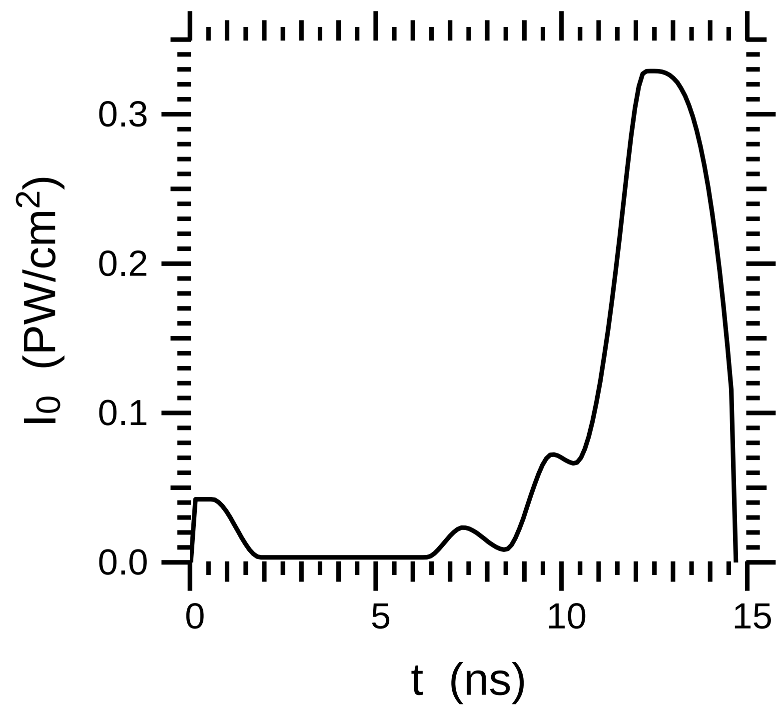

Figure 8: Nominal intensity at best focus for 285 eV NIF ignition design (“NIF example”), found by dividing the laser power per quad by the focal spot size. The peak intensity corresponds to 6.9 TW/quad.

Figure 7: (Color online.) (a) SBS reflectivity for Omega experiments

to several approaches. These include averaging the gain, finding the maximum gain, or averaging e^{G_l}. This last method stems from assuming there is no pump depletion and noise sources are independent of scattered frequency; in this limit, the reflectivity should be roughly proportional to e^{G_l}. However, this averaging, and a fortiori taking the maximum, can be dominated by gains that are unphysically larger than allowed by pump depletion or other nonlinearity. One can attempt to include pump depletion via a Tang formula for G_l at each ω_1 [25].

DEPLETE allows for more physical ray-averaging schemes. To the extent the transverse intensity pattern of a cone is uniform, each ray should be taken to represent the same incident laser power. Averaging DEPLETE's ray reflectivities then measures the fraction of incident power that gets reflected. Pump depletion is of course included, which limits backscatter along high-gain rays in a physical way. The reflectivities and scattered spectra plotted here are simple averages over the rays.

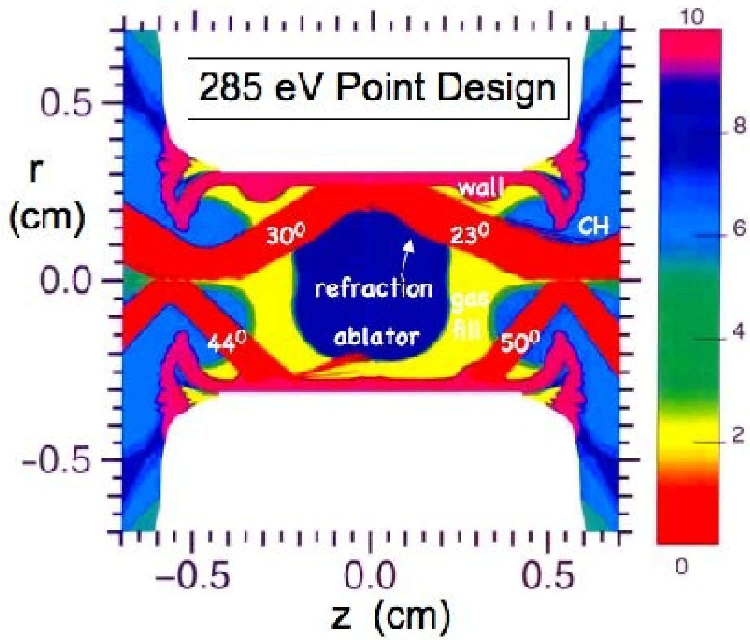

Figure 9: (Color online.) Materials and laser beam cones for NIF example.

The ray-averaged reflectivities for several times near peak laser power, for the 30° cone, are shown in Fig. 10. The results for three different cases are presented. First, the solid lines give the reflectivities computed with the unmodified DEPLETE equations. To quantify the role of re-absorption of scattered light in the target, we re-ran DEPLETE with $\kappa_1 = 0$. This leads to the dashed lines. Finally, to bound the enhancement due to speckles, we plot the results when Γ_1 is doubled (and $\kappa_1 \neq 0$) as the dotted lines.

The spectra of escaping SRS and SBS light (averaged over rays) are shown in Fig. 11-12. The SBS feature at a wavelength shift of 5-8 Å comes from the Be ablator blowoff. A much weaker feature appears from 12-13 ns at 12-15 Å, and occurs in the gas fill. The SRS spectrum is more irregular, showing two main features separated by ≈20 nm that move to higher λ_1 as time increases. In addition, there are narrow features at higher λ_1 that originate near the hohlraum wall; these would be reduced in a ray-averaged gain, since the exact λ_1 active for each ray depends sensitively on conditions near the wall and therefore varies from ray to ray. Re-absorption strongly suppresses these high-λ_1 spikes, as is seen in the SRS spectra with and without re-absorption at $t = 13.75$ ns in Fig. 13.

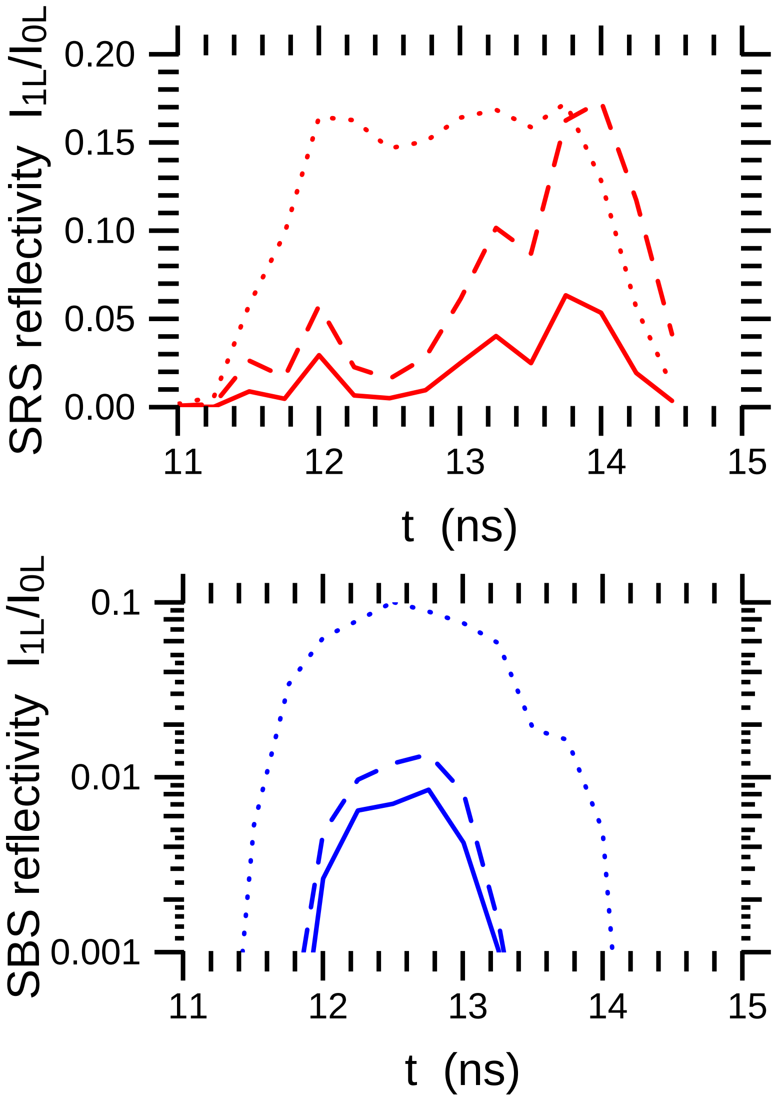

Figure 10: (Color online.) DEPLETE SRS and SBS ray-averaged reflectivities I_{1L} for NIF example. Solid lines are the nominal case (re-absorption and Γ_1 unscaled), dashed lines are the nominal Γ_1 but no re-absorption of scattered light ($\kappa_1 = 0$), and dotted lines are $2 \times \Gamma_1$ with re-absorption.

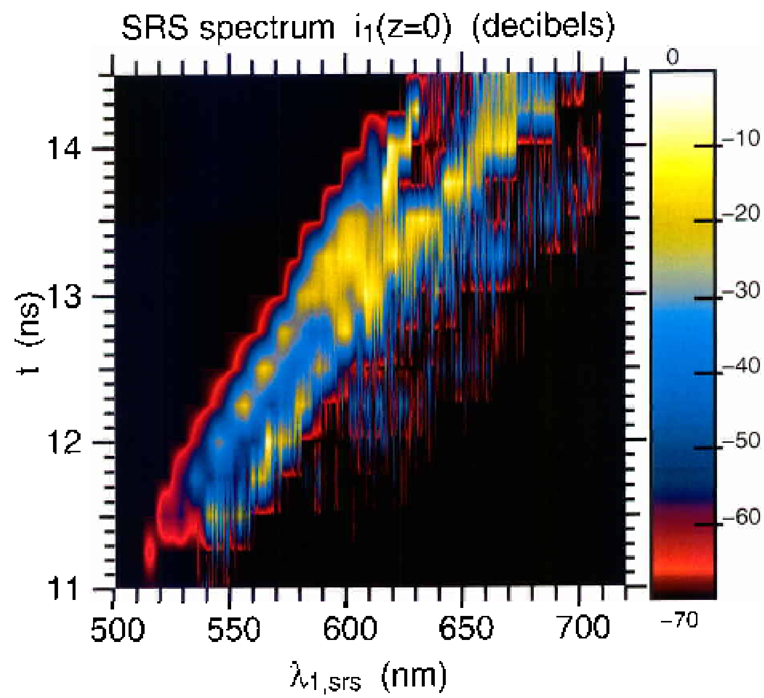

Figure 11: (Color online.) SRS streaked spectrum i_{1L} for NIF example, nominal case ($\kappa_1 \neq 0$, $1 \times \Gamma_1$).

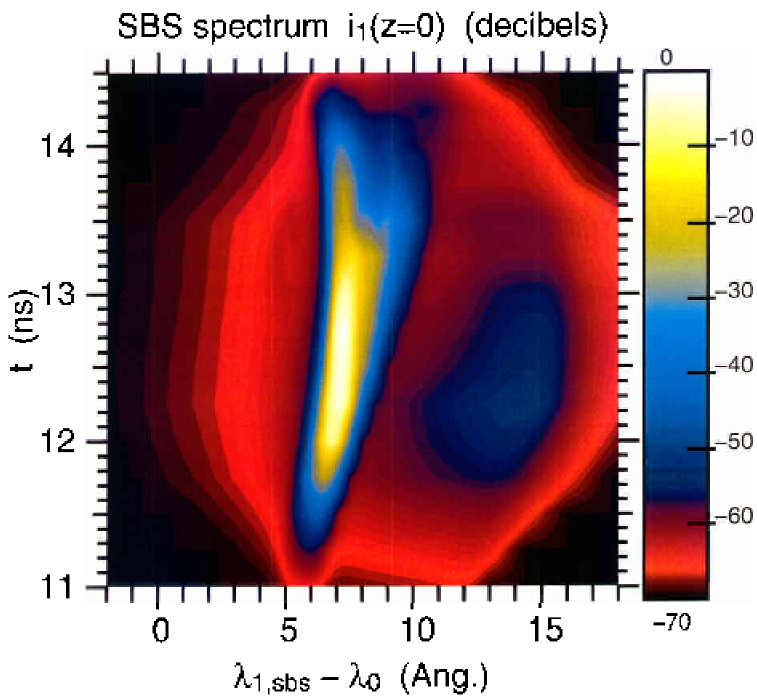

Figure 12: (Color online.) SBS streaked spectrum for NIF example, nominal case ($\kappa_1 \neq 0$, $1 \times \Gamma_1$). The white-yellow streak from 5-8 Å occurs in the Be ablator, while the weaker feature from 12-15 Å occurs in the gas fill.

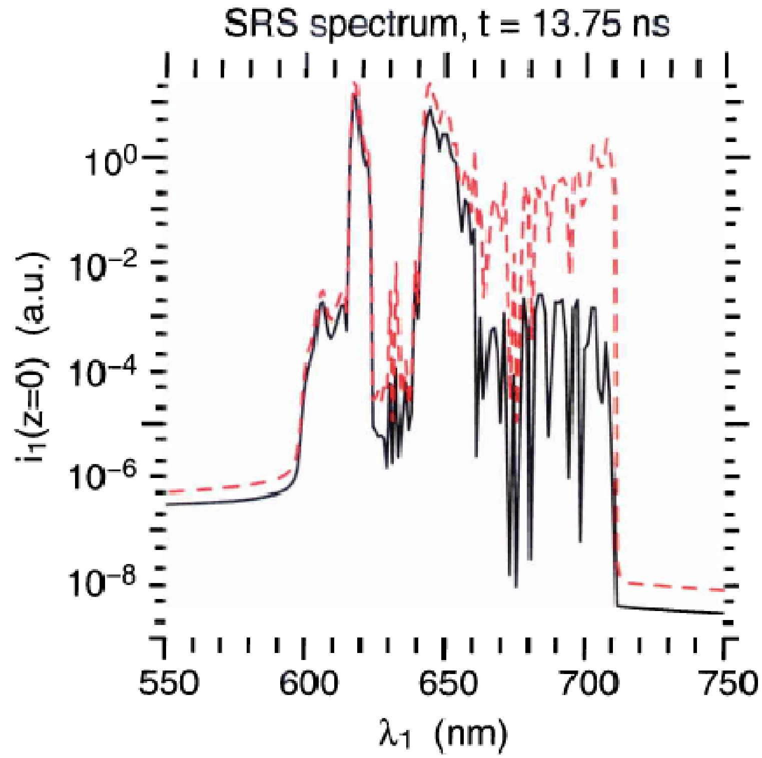

Figure 13: (Color online.) DEPLETE SRS spectrum at time 13.75 ns for NIF example, smoothed over ≈ 1 nm. The black solid and red dashed lines are computed with ($\kappa_1 \neq 0$) and without ($\kappa_1 = 0$) re-absorption of scattered light, respectively.

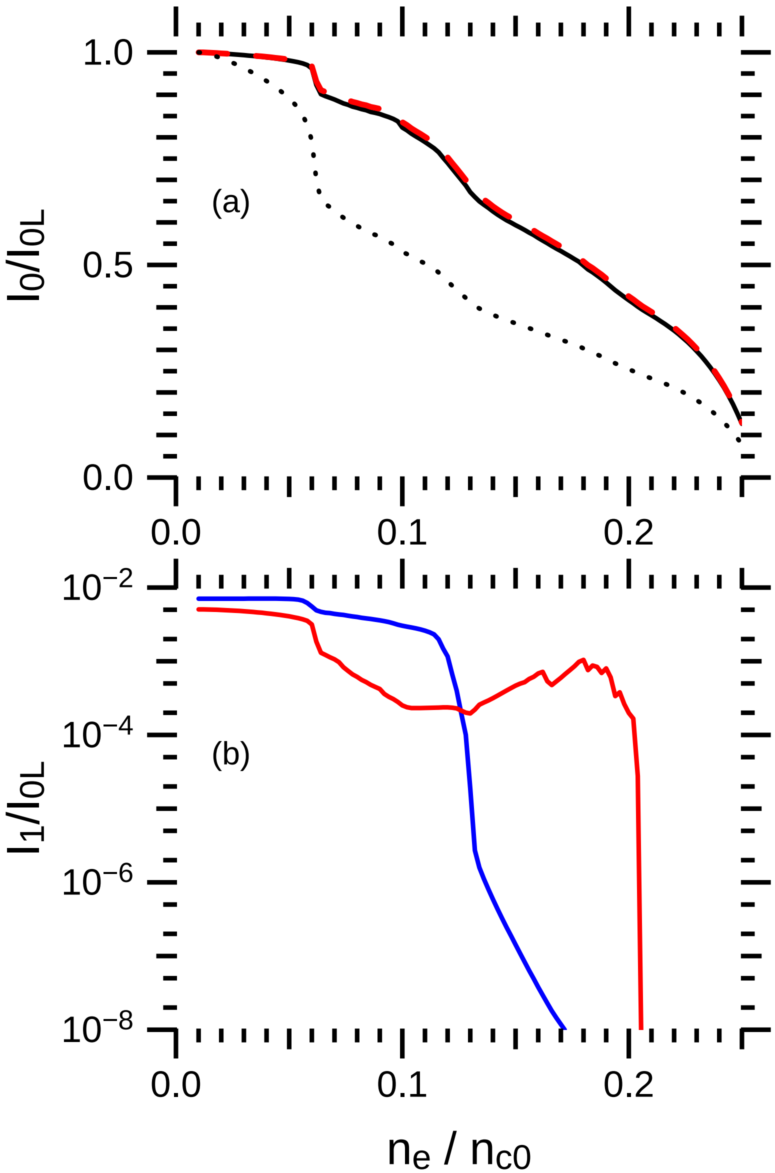

Figure 14: (Color online.) (a) Laser transmission for NIF example at 12.5 ns (peak power): black solid curve is the nominal DEPLETE solution with pump depletion, dashed red curve is with just inverse-bremsstrahlung absorption, and black dotted curve is the DEPLETE solution with $2\times\Gamma_1$. (b) SBS (blue) and SRS (red) scattered intensities for the nominal DEPLETE solution. Calculation of intensity at a given n_e is described in text.

Besides backscatter, DEPLETE also provides the pump intensity $I_0(z)$ along each ray. This indicates how much laser energy is transmitted to a given location, which is a crucial aspect of a whether LPI degrades target performance. In cases where the backscattered light undergoes significant absorption as it propagates out of the target (as happens to SRS for the design analyzed here), the measured reflectivity can understate the level of LPI. The laser transmission can reveal this fact. Figure 14(a) presents I_0, averaged over all the rays, at a given n_e. This is a 1D presentation of how much energy reaches a given density, although in the full 3D geometry different rays reach the same n_e at different locations. I_0 with just pump absorption, as well as the DEPLETE solutions with pump depletion for the nominal case and $2\times\Gamma_1$, are shown. Pump depletion is barely discernible in the nominal case, but is significant in the $2\times\Gamma_1$ case. For instance, in the latter case I_0 at $n_e/n_{c0}=0.2$ is only 60% of its absorption-only value. The wavelength-integrated SRS and SBS are shown in Fig. 14(b), and the scattered spectra vs. n_e are shown in Figs. 15-16. SRS in particular develops at several different densities, corresponding to different wavelengths, as can be seen in Figs. 13 and 15.

8 Conclusions and future prospects

We have derived a steady-state, kinetic model for Brillouin and Raman backscatter along a ray path, that includes pump depletion, bremsstrahlung damping and fluctuations, and Thomson scattering. This model is implemented by the code DEPLETE, which we have presented as well. This work extends linear gain calculations, by including more physics while retaining the low computational cost of ray-based methods. In particular, DEPLETE provides the scattered-light spectrum and intensity developing from physical noise, which can be compared against more sophisticated codes and experiments. The transmitted pump laser along the ray is also found, which is important for assessing an ICF target design, especially when re-absorption of scattered light reduces the escaping backscatter from the "intrinsic" backscatter level.

We presented benchmarks of DEPLETE on contrived, linear profiles, as well as analysis of Omega experiments and a NIF ignition design.

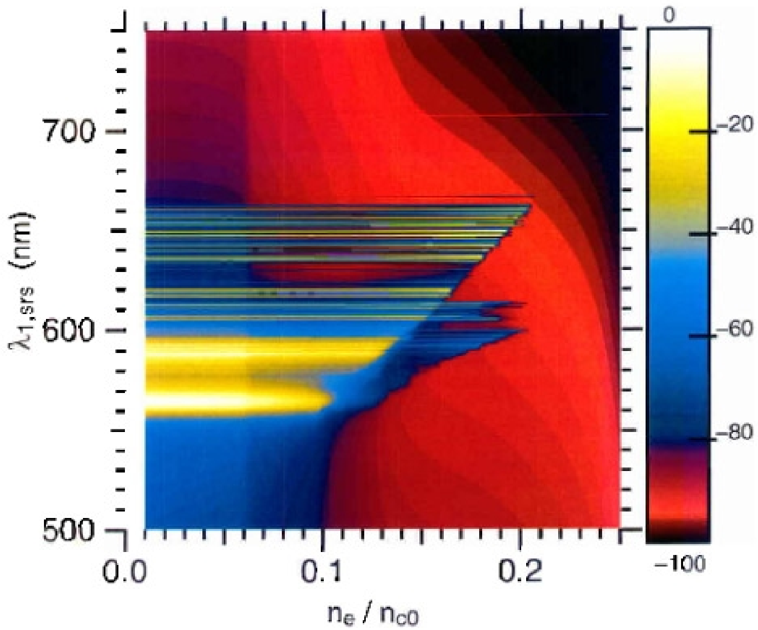

Figure 15: (Color online.) SRS spectral density i_1 vs. n_e/n_{c0} and λ_1, in decibels, at 12.5 ns (peak power), for NIF example.

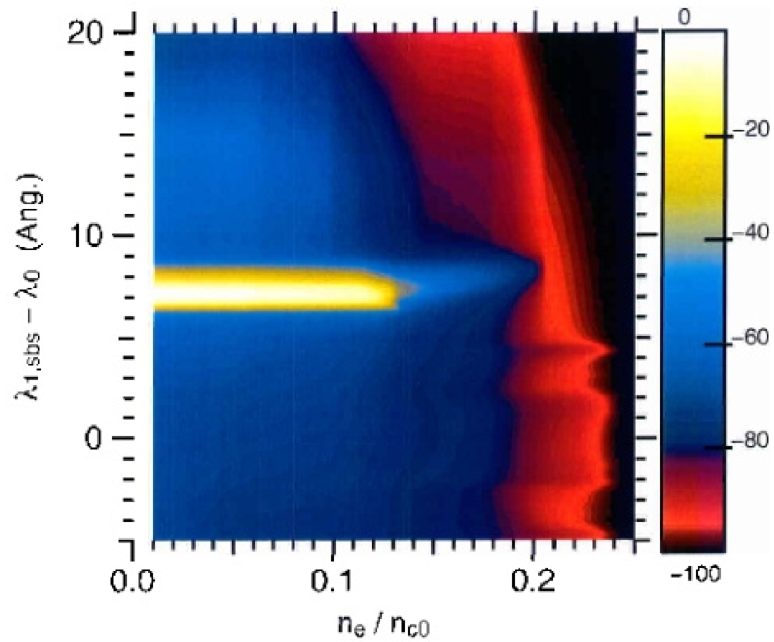

Figure 16: (Color online.) SBS spectral density i_1 vs. n_e/n_{c0} and $\lambda_1 - \lambda_0$, in decibels, at 12.5 ns (peak power), for NIF example.

The benchmarks reveal the deficiencies of linear gain, namely the neglect of TS, pump depletion, and re-absorption. Comparisons with pF3D provide a cross-validation of the two codes in a regime where they should agree. The Omega SBS experimental data, as well as pF3D simulations of these shots, show much more reflectivity than DEPLETE gives, for intensities where pump depletion is weak. This enhancement is due to speckle effects. We showed an upper bound on this enhancement is given by doubling the DEPLETE coupling coefficient Γ_1, which comes from considering the phase-conjugated mode in an RPP-smoothed beam. The ignition design analysis gives reasonably low backscatter levels for the nominal laser intensity and including re-absorption, with SRS dominating SBS. However, if re-absorption is neglected, or especially if Γ_1 is doubled to bound speckle effects, the backscatter appears more worrisome. The transmitted laser profile supports these conclusions.

Ray-based gain calculations have been used for some time to model LPI experiments. An early example for hohlraum targets is Ref. [38], where hohlraums filled with CH gas were driven by laser beams with and without PS and SSD. Without SSD, decent agreement was found between measurments and the time-dependent SBS gain spectrum. However, there was a large difference in wavelength of peak SRS between the measurements and the gain spectrum, which may be due to laser filamentation changing the location of peak SRS growth. DEPLETE can shed light on experiments like these by including more physics than gain, and giving absolute levels of reflected and transmitted light.

Several future directions exist for enhancing DEPLETE. A superior approach to include speckle effects, than the $2 \times \Gamma_1$ method discussed in this paper, is to solve the DEPLETE equations over a speckle length, for a distribution of pump intensities chosen to obey the known speckle statistics, and then re-distribute the power (since the speckle pattern changes over a speckle length). This would require some changes to the code, and multiply the time needed to solve the ODEs by the number of pump intensities considered. However, since the overall run time is dominated by computing coefficients (specifically the Z function in χ_j), the runtime will not change as much. Including speckles, even approximately, in a ray-based code should be pursued due to the much lower computational cost compared to propagation codes like pF3D.

DEPLETE also enables some new diagnostics and applications. The pump and scattered intensities found by DEPLETE can be used to compute the local material heating rate due to absorption. Since this is the prime way the laser affects matter in radiation hydrodynamics, one could incorporate our ray-based model into a hydrodynamic code. This would couple laser-plasma interactions to target evolution in a self-consistent, if simplified, way. In addition, the plasma-wave amplitudes found by DEPLETE can be compared against thresholds for various nonlinearities to assess their relevance, and may allow estimation of hot electron production by SRS.

Despite its promise, there are limits inherent to any ray-based approach. Namely, any physical connection between different rays (as found via geometric optics) is neglected. Therefore, changes in the pump laser such as filamentation, beam spray, and beam bending cannot be accounted for. In addition, the facts that backscattered light (particularly SRS) does not follow the same refracted path as the pump, and that backscatter is sensitive to transverse plasma profiles, are ignored. A 3D ray-based approach may be able to include these effects, although the computational cost may approach that of a more complete paraxial description. Such a code, called SLIP, is being developed, which like DEPLETE operates in steady state and uses kinetic coefficients [22]. This model is in some sense intermediate between DEPLETE and pF3D.

Even given these more advanced tools, ray-based codes like DEPLETE have a valuable role. They can analyze a single ray, using hundreds of scattered wavelengths, in a few seconds, thus allowing designs to be analyzed for many times steps and over many rays in a routine way. The resulting spectra allow for contact with experimental diagnostics like spectra, and are frequently needed to choose, e.g., the carrier k and ω for pF3D. Ray-based analyses also provide qualitative guidance about how certain changes in a design change the LPI.

Laser-plasma interactions have proven to be a very challenging area of plasma physics, owing to the variety of relevant physics and extreme range of scales involved. This has led to an equally extreme range of modeling tools, from ray-based gain estimates to 3D kinetic simulations. By fully exploiting these tools, each with their uses and limitations, a more complete picture is emerging.

A newlip

In this appendix, we document the laser interaction post-processor NEWLIP, of which DEPLETE can be viewed as an extension. The equations underlying NEWLIP are

$$\begin{aligned} d_z I_0(z) &= -\kappa_0 I_0, && (77)\\ \partial_z i_1(z,\omega_1) &= -I_0\Gamma_1 i_1. && (78)\end{aligned}$$

The first of these is Eq. (55) with no pump depletion ($\tau_1 = \Gamma_1 = 0$), and the second is Eq. (56) with no bremsstrahlung or TS ($\kappa_1 = \Sigma_1 = \tau_1 = 0$). That is, only the absorption of the pump, and coherent coupling to scattered light waves, are modeled. The boundary conditions are $I_0(z=0) = I_{0L}$ (the known pump at the laser entrance), and $i_1(z = L_z, \omega_1) = 1$. We thus solve for a unit scattered-wave boundary seed, which is permissible for this linear system.

We readily solve Eqs. (77-78) to find

$$\begin{aligned} I_0(z) &= I_{0L} e^{-\int_0^z dz'\ \kappa_0(z')}, && (79)\\ i_1(z) &= e^{G_l(z)}, && (80)\\ G_l(z) &\equiv \int_z^{L_z} dz'\ \Gamma_1(z')I_0(z'). && (81)\end{aligned}$$

$G_l(z)$ is the linear intensity gain exponent, and is the main result of NEWLIP used to characterize the backscatter level of a target design. The total gain across the profile is $G_l(z=0)$.

The numerical computation of G_l suffers from the problem of narrow resonances, similar to DEPLETE. The coupling coefficient Γ_1 (see Eq. (24)) is sharply peaked near the resonance point where $\mathrm{Re}\,\epsilon = 0$. NEWLIP addresses this challenge in a way analogous to how DEPLETE handles the coupling-Thomson step, as outlined in Appendix B. In particular, the integration of Eq. (78) from z^n down to z^{n-1} can be cast in the form

$$\ln\frac{i_1^{n-1}}{i_1^n} = \mathrm{Im}\, S_0, \qquad S_0 \equiv \int_{z^n}^{z^{n-1}} dz\ \frac{S}{\epsilon}, \qquad (82)$$

with $S \equiv -I_0 f \Gamma_S \chi_e(1+\chi_I)$. Although $S(z)/\epsilon(z)$ is sharply-peaked near resonance, $S(z)$ and $\epsilon(z)$ are themselves slowly-varying with z. We approximate $S(z) \approx S^{n-1/2} + (z - z^{n-1/2})\Delta S/\Delta z$ (and similarly for ϵ), with $X^{n-1/2} \equiv (X^n + X^{n-1})/2$ and $\Delta X \equiv (X^n - X^{n-1})$ for some quantity X . With this representation, and $\hat{X} \equiv X^{n-1/2}/\Delta X$, we find

$$S_0 = \frac{\Delta z \Delta S}{\Delta \epsilon}\left[1 + (\hat{\epsilon} - \hat{S})\ln\frac{\epsilon^{n-1}}{\epsilon^n}\right]. \qquad (83)$$

This formula is valid provided either $|\mathrm{Re}\,\hat{\epsilon}| \geq 1/2$ or $\mathrm{Im}\,\hat{\epsilon} \neq 0$. For accuracy, we also want $\Delta\epsilon$ to not be too small (which obtains, e.g., for a flat profile). We therefore require $|\hat{\epsilon}|$ to be less than some large number. If any of these conditions does not hold, we simply assume $S = S^{n-1/2}$ and $\epsilon = \epsilon^{n-1/2}$ across the cell to find

$$S_0 = \Delta z \frac{S^{n-1/2}}{\epsilon^{n-1/2}}. \qquad (84)$$

B Numerical solution of the coupling-Thomson step

This appendix provides a derivation of Eq. (69), the solution for i_1 in the coupling-Thomson step. We must solve Eq. (62), from z^n down to z^{n-1}, with $I_0 = I_0^n$ and all coefficients *except* $|\epsilon|^2$ evaluated at $z^{n-1/2}$. We write this equation as

$$\begin{aligned} \partial_z i_1 &= -\frac{K_\tau + K_\Gamma i_1}{|\epsilon|^2}, && (85)\\ K_\tau &\equiv I_0^n \tau_S^{n-1/2} g_\tau^{n-1/2}, \qquad K_\Gamma \equiv I_0^n \Gamma_S^{n-1/2} g_\Gamma^{n-1/2}. && (86)\end{aligned}$$

As mentioned above, the principal numerical difficulty is that $|\epsilon|^{-2}$ is sharply peaked near resonance ($\mathrm{Re}\,\epsilon = 0$). This rapid variation in the coefficients of Eq. (85) requires very fine z meshing to correctly resolve with a standard ODE solver. However, the rapid variation in $|\epsilon|^{-2}$ arises from the generally gradual passage of $\mathrm{Re}\,\epsilon$ through zero. We exploit this fact to Taylor expand ϵ within each zone, and solve the resulting system analytically.

Define the zonal average and difference $X^{n-1/2} \equiv (1/2)(X^n + X^{n-1})$ and $\Delta X \equiv X^n - X^{n-1}$ for the quantity X. We expand ϵ about the zone center $z^{n-1/2}$ to find

$$\begin{aligned} \epsilon &\approx \epsilon^{n-1/2} + \hat{z}\Delta\epsilon, & (87) \\ \hat{z} &\equiv \frac{z - z^{n-1/2}}{\Delta z}. & (88) \end{aligned}$$

We can then write

$$\begin{aligned} |\epsilon|^2 &= \epsilon_1 + |\Delta\epsilon|^2(\hat{z} - \hat{z}_0)^2, & (89) \\ \epsilon_1 &\equiv |\Delta\epsilon|^{-2}\mathrm{Im}\left[\epsilon^{n-1/2}\Delta\epsilon^*\right]^2, & (90) \\ \hat{z}_0 &\equiv -|\Delta\epsilon|^{-2}\mathrm{Re}\left[\epsilon^{n-1/2}\Delta\epsilon^*\right]. & (91) \end{aligned}$$

The linear change of variable

$$s \equiv \frac{|\Delta\epsilon|}{\sqrt{\epsilon_1}}(\hat{z} - \hat{z}_0) \quad (92)$$

transforms Eq. (85) to

$$\begin{aligned} \partial_s i_1 &= -\frac{B_\tau + B_\Gamma i_1}{1 + s^2}, & (93) \\ B_{\tau,\Gamma} &\equiv \frac{K_{\tau,\Gamma}\Delta z}{\left|\mathrm{Im}\left[\epsilon^{n-1/2}\Delta\epsilon^*\right]\right|}. & (94) \end{aligned}$$

A second change of variable to $w \equiv \mathrm{atan}\ s$ yields

$$\partial_w i_1 = -(B_\tau + B_\Gamma i_1). \quad (95)$$

This equation is readily solvable, and gives the solution used above in Eq. (69):

$$\begin{aligned} i_1^{n-1} &= (i_1^n + i_\tau)e^{B_\Gamma \Delta w_n} - i_\tau, & (96) \\ \Delta w_n &\equiv \mathrm{atan}\ s^n - \mathrm{atan}\ s^{n-1}. & (97) \end{aligned}$$

$i_\tau = B_\tau/B_\Gamma$ is also given by Eq. (53).

If $\Delta\epsilon$ is sufficiently small (or zero, as for a flat profile), we do not use Eq. (87), but instead $\epsilon \approx \epsilon^{n-1/2}$. We can then immediately solve Eq. (85) to find

$$i_1^{n-1} = (i_1^n + i_\tau)\exp\left[K_\Gamma|\epsilon^{n-1/2}|^{-2}\Delta z\right] - i_\tau. \quad (98)$$

References

[1] William L. Kruer. *The Physics of Laser Plasma Interactions.* Westview Press, Boulder, CO, 2003.

[2] T. Tajima and J. M. Dawson. Laser electron accelerator. *Phys. Rev. Lett.*, 43(4):267–270, Jul 1979.

[3] V. M. Malkin, G. Shvets, and N. J. Fisch. Fast compression of laser beams to highly overcritical powers. *Phys. Rev. Lett.*, 82(22):4448–4451, 1999.

[4] S. Atzeni and J. Meyer ter Vehn. *The Physics of Inertial Fusion: Beam Plasma Interaction, Hydrodynamics, Hot Dense Matter.* Oxford University Press, Oxford, UK, 2004.

[5] John Lindl, Peter Amendt, Richard L. Berger, S. Gail Glendinning, Siegfried H. Glenzer, Steven W. Haan, Robert L. Kauffman, Otto L. Landen, and Laurence J. Suter. The physics basis for ignition using indirect-drive targets on the national ignition facility. *Phys. Plasmas*, 11:339–491, 2004.

[6] R. L. Berger, E. A. Williams, and A. Simon. Effect of plasma noise spectrum on stimulated scattering in inhomogeneous plasma. *Phys. Fluids B*, 1(2):414–421, 1989.

[7] A. Ramani and C. E. Max. Stimulated brillouin scattering in an inhomogeneous plasma with broad-bandwidh thermal noise. *Phys. Fluids*, 26(4):1079–1102, 1983.

[8] Philippe Mounaix, Denis Pesme, and Michel Casanova. Nonlinear reflectivity of an inhomogeneous plasma in the strongly damped regime. *Phys. Rev. E*, 55(4):4653–4664, 1997.

[9] E. A. Williams. ICF Annual Report, LLNL, 1998.

[10] D. H. Froula, L. Divol, N. B. Meezan, S. Dixit, J. D. Moody, P. Neumayer, B. B. Pollock, J. S. Ross, and S. H. Glenzer. Ideal laser-beam propagation through high-temperature ignition hohlraum plasmas. *Phys. Rev. Lett.*, 98(8):085001, 2007.

[11] P. Neumayer, R. L. Berger, L. Divol, D. H. Froula, R. A. London, B. J. MacGowan, N. B. Meezan, J. S. Ross, C. Sorce, L. J. Suter, and S. H. Glenzer. Suppression of stimulated brillouin scattering by increased landau damping in multiple-ion-species hohlraum plasmas. *Phys. Rev. Lett.*, 100(10):105001, 2008.

[12] T. R. Boehly, D. L. Brown, R. S. Craxton, R. L. Keck, J. P. Knauer, J. H. Kelly, T. J. Kessler, S. A. Kumpan, S. J. Loucks, S. A. Letzring, F. J. Marshall, R. L. McCrory, S. F. B. Morse, W. Seka, J. M. Soures, and C. P. Verdon. Initial performance results of the omega laser system. *Opt. Commun.*, 133:495–506, January 1997.

[13] Thierry Dewandre, James R. Albritton, and E. A. Williams. Doppler shift of laser light reflected from expanding plasmas. *Phys. Fluids*, 24(3):528–536, 1981.

[14] A. Bers. Linear waves and instabilities. In C. DeWitt and J. Peyraud, editors, *Physique des Plasmas - Les Houches 1972*. Gordon and Breach, New York, 1975.

[15] Bruce I. Cohen and Allan N. Kaufman. Nonlinear plasma waves excited near resonance. *Phys. Fluids*, 20:1113–1117, 1977.

[16] B. D. Fried and S. D. Conte. *The Plasma Dispersion Function: The Hilbert Transform of the Gaussian*. Academic Press, New York, 1961.

[17] M. Abramowitz and I. A. Stegun. *Handbook of Mathematical Functions*. Dover Publications, Inc., New York, NY, 1970.

[18] G. Bekefi. *Radiation Processes in Plasmas*. John Wiley and Sons, New York, 1966.

[19] John Dawson and Carl Oberman. High-frequency conductivity and the emission and absorption coefficients of a fully ionized plasma. *Phys. Fluids*, 5(5):517–524, 1962.

[20] C. R. Oberman and E. A. Williams. Theory of fluctuations in plasma. In M. N. Rosenbluth and R. Z. Sagdeev, editors, *Handbook of Plasma Physics, Vol. 1*, chapter 2.3. North-Holland, Amsterdam, 1983.

[21] D. E. Evans. The effect of impurities on the spectrum of laser light scattered by a plasma. *Plasma Phys.*, 12:573–584, 1970.

[22] D. H. Froula, L. Divol, R. A. London, P. Michel, R. L. Berger, N. B. Meezan, P. Neumayer, J. S. Ross, R. Wallace, and S. H. Glenzer. Pushing the limits of plasma length in inertial-fusion laser-plasma interaction experiments. *Phys. Rev. Lett.*, 100(1):015002, 2008.

[23] Gilbert Strang. On the construction and comparison of difference schemes. *SIAM J. Numer. Anal.*, 5(3):506–517, 1968.

[24] N. N. Yanencko. *The Method of Fractional Steps*. Springer-Verlag, New York, 1970.

[25] C. L. Tang. Saturation and spectral characteristics of the stokes emission in the stimulated Brillouin process. *J. Appl. Phys.*, 37(8):2945–2955, 1966.

[26] R. L. Berger, C. H. Still, E. A. Williams, and A. B. Langdon. On the dominant and subdominant behavior of stimulated raman and brillouin scattering driven by nonuniform laser beams. *Phys. Plasmas*, 5(12):4337–4356, 1998.

[27] D. H. Froula, L. Divol, N. B. Meezan, S. Dixit, P. Neumayer, J. D. Moody, B. B. Pollock, J. S. Ross, L. Suter, and S. H. Glenzer. Laser beam propagation through inertial confinement fusion hohlraum plasmas. *Phys. Plasmas*, 14(5):055705, 2007.

[28] S. N. Dixit, M. D. Feit, M. D. Perry, and H. T. Powell. Designing fully continuous phase screens for tailoring focal-plane irradiance profiles. *Opt. Lett.*, 21(21):1715, 1996.

[29] D. H. Froula, J. S. Ross, L. Divol, N. Meezan, A. J. MacKinnon, R. Wallace, and S. H. Glenzer. Thomson-scattering measurements

of high electron temperature hohlraum plasmas for laser-plasma interaction studies. *Phys. Plasmas*, 13(5):052704, 2006.

[30] M. M. Marinak, G. D. Kerbel, N. A. Gentile, O. Jones, D. Munro, S. Pollaine, T. R. Dittrich, and S. W. Haan. Three-dimensional hydra simulations of national ignition facility targets. *Phys. Plasmas*, 8(5):2275–2280, 2001.

[31] N. B. Meezan, R. L. Berger, L. Divol, D. H. Froula, D. E. Hinkel, O. S. Jones, R. A. London, J. D. Moody, M. M. Marinak, C. Niemann, P. B. Neumayer, S. T. Prisbrey, J. S. Ross, E. A. Williams, S. H. Glenzer, and L. J. Suter. Role of hydrodynamics simulations in laser-plasma interaction predictive capability. *Phys. Plasmas*, 14(5):056304, 2007.

[32] L. Divol, R. L. Berger, N. B. Meezan, D. H. Froula, S. Dixit, P. Michel, R. London, D. Strozzi, J. Ross, E. A. Williams, B. Still, L. J. Suter, and S. H. Glenzer. Three-dimensional modeling of laser-plasma interaction: Benchmarking our predictive modeling tools versus experiments. *Phys. Plasmas*, 15(5):056313, 2008.

[33] B. Ya. Zel'dovich, N. F. Pilipetsky, and V. V. Shkunov. *Principles of Phase Conjugation*. Springer-Verlag, Berlin, 1985.

[34] Laurent Divol, E. A. Wiliams, R. L. Berger, and D. E. Hinkel. Reduction of backscatter in long plasma with beam smoothing in the moderate gain regime. *Bull. Am. Phys. Soc.*, 50(8), 2005.

[35] G. Zimmerman and W. L. Kruer. junk. *Comments Plasma Phys. Controlled Fusion*, 2:85, 1975.

[36] D. A. Callahan, D. E. Hinkel, R. L. Berger, L. Divol, S. N. Dixit, et al. Optimization of the nif ignition point design hohlraum. *IFSA 2007 proceedings, Journ. Physics: Conference Series*, 2008.

[37] D. E. Hinkel, D. A. Callahan, A. B. Langdon, S. H. Langer, C. H. Still, and E. A. Williams. Analyses of laser-plasma interactions in national ignition facility ignition targets. *Phys. Plasmas*, 15:056314, 2008.

[38] S. H. Glenzer, R. L. Berger, L. M. Divol, R. K. Kirkwood, B. J. MacGowan, J. D. Moody, A. B. Langdon, L. J. Suter, and E. A. Williams. Reduction of stimulated scattering losses from hohlraum plasmas with laser beam smoothing. *Phys. Plasmas*, 8(5):1692–1696, 2001.